KfK 4921
CNEA NT-1/91
Juli 1992

Analysis and Modelling of the Chemical Interactions Between Inconel Grid Spacers and Zircaloy Cladding of LWR Fuel Rods; Formation of Liquid Phases due to Chemical Interactions

E. A. Garcia, P. Hofmann, A. Denis
Institut für Materialforschung
Projekt Nukleare Sicherheitsforschung
Departamento de Combustibles Nucleares, CNEA/CAC
Buenos Aires, Argentina

Kernforschungszentrum Karlsruhe

Kernforschungszentrum Karlsruhe
Institut für Materialforschung
Projekt Nukleare Sicherheitsforschung

Departamento de Combustibles Nucleares
Comisión Nacional de Energía Atómica
Buenos Aires, Argentina

KfK 4921
CNEA NT-1/91

Analysis and Modelling of the Chemical Interactions Between Inconel Grid Spacers and Zircaloy Cladding of LWR Fuel Rods; Formation of Liquid Phases due to Chemical Interactions

E. A. Garcia

P. Hofmann

A. Denis

in cooperation with

M. Markiewicz*

*CNEA/CAC

Kernforschungszentrum Karlsruhe GmbH, Karlsruhe

Kernforschungszentrum Karlsruhe GmbH
Postfach 3640, 7500 Karlsruhe 1

ISSN 0303-4003

SUMMARY

As a result of the SFD CORA (Severe Fuel Damage) experiments (LWR bundle tests) the formation of liquid phases was observed as a consequence of chemical interactions between the various bundle components below their melting points. The reaction kinetics of the different material combinations has been studied. One of them, the chemical interaction between the Inconel of the spacer grids and Zircaloy fuel rod cladding, will be described in this work.

The experimental results show that the interactions obey parabolic rate laws at the examined temperatures of 1000, 1100 and 1200°C, with or without preoxidized Zircaloy. The fundamental difference of the experiments with preoxidized Zircaloy (oxide layer thickness $\leq 100\mu m$) compared to as-received Zircaloy is the time delay of the start of the interaction between Inconel and Zircaloy.

Two models will be presented to describe the experimental results: a) the DISOL code, which is able to simulate the oxidation of Zircaloy up to a given oxide layer thickness and then the dissolution of the ZrO_2 layer by the Zircaloy, and b) the solid/ solid interaction model that is able to describe the kinetics of the Inconel/Zircaloy interaction. The simple relations obtained as a result of this work can be introduced as modules in SFD code systems to describe the behavior of the core with increasing temperature. Comparison between the experimental results and the code predictions shows a good agreement.

CHEMISCHE WECHSELWIRKUNGEN ZWISCHEN INCONEL-ABSTANDSHALTERN UND BRENNELEMENT-HÜLLROHREN AUS ZIRCALOY; BILDUNG FLÜSSIGER PHASEN INFOLGE CHEMISCHER WECHSELWIRKUNGEN UND DEREN MODELLIERUNG

Zusammenfassung

Die CORA-Experimente zum Brennelementverhalten bei hohen Temperaturen ergaben die Bildung von flüssigen Phasen infolge chemischer Wechselwirkungen der verschiedenen Bündelkomponenten miteinander, z.T. weit unterhalb ihrer Schmelzpunkte. Die Reaktionskinetik der verschiedenen Materialkombinationen wurde experimentell ermittelt. Die chemischen Wechselwirkungen zwischen Inconel-Abstandshalter und LWR- Brennelement-Hüllrohren aus Zircaloy-4 und deren modellmäßige Beschreibung ist Thema dieses Berichts.

Die experimentellen Versuchsergebnisse zeigen, daß die Wechselwirkungen für die untersuchten Temperaturen von 1000, 1100 und 1200°C mittels eines parabolischen Zeitgesetzes beschrieben werden können. Dies gilt für Zircaloy-Hüllrohre ohne und mit Oxidschichten. Der wesentliche Unterschied in den Experimenten mit voroxidiertem Zircaloy ($\leq 100 \mu m$ ZrO_2) im Vergleich zu den nicht oxidierten Proben ist, daß der Reaktionsbeginn zwischen Inconel und Zircaloy verzögert wird, da sich die Oxidschicht erst chemisch auflösen muß.

Es werden zwei Modelle dargestellt, die die experimentellen Ergebnisse beschreiben: a) der DISOL Code, der in der Lage ist, die Oxidation von Zircaloy bis zu einer bestimmten Oxidschichtdicke und die nachfolgende ZrO_2-Auflösung durch das Zircaloy zu beschreiben und b) ein Modell zur Beschreibung der chemischen Wechselwirkungen zwischen Inconel und Zircaloy. Die ermittelten einfachen Beziehungen können in SFD- (Severe Fuel Damage) Rechenprogrammen zur Beschreibung des Coreverhaltens mit steigender Temperatur als Module eingesetzt werden. Der Vergleich zwischen den experimentellen Ergebnissen und denen der Berechnungen zeigt eine gute Übereinstimmung.

CONTENTS

Page

Summary

1. INTRODUCTION

In severe reactor accidents, the temperature within the core exceeds 1200°C, which is the maximum tolerable temperature for design-basis accidents. At these high temperatures the various materials of the fuel-rod bundles chemically interact with each other and with the steam of the environment. Of special interest with respect to damage initiation and progression are the eutectic interactions since they result in the formation of liquid phases at low temperatures. Experiments with fuel rod bundles, which were heated up to 2000°C, clearly show by optical observations and temperature measurements that liquid phases form and relocate far below the melting point of the components [1,2]. In PWRs, the low-temperature melting of the (Ag,In,Cd) absorber alloy, at about 800°C, will not affect core degradation as long as the molten material is contained within the stainless steel cladding. After chemical or/and mechanical failure of the stainless steel cladding the released absorber alloy interacts with the Zircaloy cladding tubes of the fuel rods and dissolves it far below its melting point at temperatures above 1200°C [3]. At this temperature the Inconel spacer grids also start to liquefy as a result of chemical interactions with Zircaloy [2,4]. These resulting liquid reaction products enhance and accelerate the degradation of the core. For this reason, it has been of great interest to study the chemical interactions in separate-effect tests [3,4] and to describe the material interactions by models which can be used in computer codes.

In this work a diffusion model is presented which is able to describe the chemical interaction between solid materials which results in the formation of a liquid phase. The model is based on physical constants like diffusion coefficients and equilibrium concentrations at the phase boundaries and is designed to simulate isothermal experiments. As an example, the chemical behavior of the Inconel spacer grids in contact with Zircaloy cladding tubes of fuel rods and absorber rod guide tubes was selected to verify the developed model. Besides, the influence on the chemical interaction of thin oxide layers on the Zircaloy surface was taken into account.

In a separate work [5] it is shown that to simulate correctly the transient behavior if diffusion processes are involved it is necessary to know the temperature dependence of the diffusion coefficients which are evaluated using the results of isothermal experiments together with a diffusion model. The parabolic rate constants, which are directly determined from the experiments, do not allow in general to simulate transient experiments. The usefullness of this procedure has already been demonstrated in [6] where the HITO code was used to simulate the high temperature interactions $UO_2/Zry/H_2O$ during transients.

2. EXPERIMENTAL RESULTS

Isothermal annealing experiments were performed with Zircaloy-4 (Zry) capsules in which short cylindrical rods of Inconel 718 (main constituents: 54wt% Ni, 18wt% Cr, 18wt% Fe, 2.9wt% Mo) were pressed and sealed gas-tight with a conical Zry plug [4].

At normal reactor operation conditions a thin oxide layer forms on the surface of Zry due to interaction with the cooling water. In addition, during high-temperature transients above 1000°C a further rapid oxidation of Zry with steam takes place. Oxide layers can prevent or delay the chemical interaction between Zry and Inconel. For this reason, the influence of ZrO_2 layers of different thicknesses (10, 20, 45 and 100μm) has been studied.

The annealing experiments were performed in a tube furnace under flowing argon. The investigated temperature ranged from 1000 to 1400°C and the maximum annealing time was 60 minutes. The highest examined temperature (1200°C for as-received Zry and 1400°C for previously oxidized Zry) was limited by the failure of the specimens due to the onset of liquid phase formation followed by a fast and complete liquefaction of the Zry crucible at slightly higher temperatures [4]. The results of the Zry/Inconel interaction experiments are described in [4]. Therefore, only a short description of the main results is given here.

After annealing, the specimens were mechanically cut and metallographically prepared for examination of the reaction zones with an optical microscope. The cross sections of Zry/Inconel reaction specimens annealed at 1000, 1100, 1150 and 1200°C for various reaction times are shown in Figure 1. The cross sections of both as-received and pre-oxidized specimens (initial ZrO_2 layer thickness of 10μm) are presented for comparison. The oxide layer on the Zry surface delays and reduces the chemical interaction between Inconel and pre-oxidized Zircaloy, but cannot prevent it.

In order to determine the Zry/Inconel reaction kinetics, the maximum increase in the crucible inner diameter or the maximum decrease in Zry wall thickness was measured as a function of temperature and time. As an example the reaction zone thicknesses produced at 1100°C are plotted as a function of time in Figure 2a for Zry and in Figure 2b for Inconel. The lines in the figures were determined by linear regression using the method of least squares.

At all the examined temperatures, the resulting reaction products were liquid at temperature since Zry and Inconel interact with each other eutectically. The lowest eutectic temperature in the (Zr-Ni) system is about 960°C on the Zr rich side, i.e. well below the lowest annealing temperature. The diffusion of approximately 3wt%Ni into Zr results in the formation of a liquid phase even at this low temperature. The liquid reaction products relocate after failure of the Zry crucible and form voids which can be recognized in Figure 1.

The isothermal growth rates for the reaction zones in Zry and Inconel obey parabolic rate laws, indicating a diffusion-controlled process. Only small amounts of Inconel are necessary to dissolve and liquefy large quantities of Zry and a complete liquefaction of the as-received specimens occurs above 1250°C.

The reaction zone growth rate equations for the Zry/Inconel interaction are:

$$K^{Zircaloy} = 46364\ \exp(-252312/RT) \quad for\ X=0\mu m$$

$$K^{Zircaloy} = 44792\ \exp(-255162/RT) \quad for\ X=20\mu m \qquad (1)$$

$$K^{Zircaloy} = 4.321x10^{9}\ \exp(-407522/RT) \quad for\ X=45\mu m$$

$$K^{Zircaloy} = 9.512\ \exp(-172165/RT) \quad for\ X=100\mu m$$

$$K^{Inconel} = 166127\ \exp(-288100/RT) \quad for\ X=0\mu m$$

$$K^{Inconel} = 1.377x10^{13}\ \exp(-504679/RT) \quad for\ X=20\mu m \qquad (2)$$

$$K^{Inconel} = 3.489x10^{19}\ \exp(-693692/RT) \quad for\ X=45\mu m$$

$$K^{Inconel} = 8941\ \exp(-253057/RT) \quad for\ X=100\mu m$$

where the gas constant R is 8.314 J/mol K, T in K, $K^{Zircaloy}$ and $K^{Inconel}$ in cm^2/s and X is the initial oxide layer thickness.
They are plotted as functions of the reciprocal temperature in Figures 3 and 4 for Zry and Inconel, respectively. The equations can be extrapolated to lower temperatures, but not to higher temperatures due to liquefaction of the specimens.

Oxide layers on the Zry surface delay and reduce the chemical interaction between Zry and Inconel. Inconel does not interact with ZrO_2, but the oxide layer will partially or totally dissolve during a time-dependent incubation period t_o. The Zry/Inconel interaction will begin either as soon as the oxide has disappeared or when short-circuit diffusion of Zr and Ni through the oxide scale has allowed these species to arrive at the opposite side of the scale. The latter mechanism has surely been effective in certain cases in which liquid layers were observed on both sides of the partially dissolved oxide layer. This fast diffusion process explains the fact that the incubation time results to be shorter than the expected one if the oxide dissolution had been completed. Figures 3 and 4 clearly demonstrate the influence of oxide layers on the liquefaction of the specimens. Moreover, the thicker the oxide layer the later the onset of liquid phase formation occurs and liquefaction will be shifted to higher temperatures (Figure 2).

In general, the reaction zone growth rates for pre-oxidized Zry are slower than for as-received Zry. The oxygen dissolved in the Zry lattice influences the diffusion and/or dissolution processes. The complete meltdown of the components will be shifted to higher temperatures (up to 1400°C) for thicker oxide layers (Figures 3 and 4).

3. THE INTERACTION MODEL

A model has been developed to describe the solid/solid interaction without oxide layer. The experimental results for preoxidized Zry will be interpreted with the same model.

3.1 The solid/solid interaction model

Inconel and Zry are considered to be in good solid contact at $t=0$ and $x=0$, with the x axis perpendicular to the contact surface. Although all the experiments are performed in a cylindrical geometry, as a first approach we can approximate the interaction surface by a plane.

Figure 5 represents the system after some time of interaction at $T \geq 1000°C$. Inconel is molten up to $-x_1$ and Zircaloy up to x_2. These two distances are experimentally determined as functions of time for each examined temperature. The eutectic formed by the interaction process is placed between $-x_1$ and x_2. On the average this eutectic has the composition that corresponds to the involved volumes x_1S and x_2S, where S is the contact surface.

As a first approximation we also assume that the total solid volume $(x_1+x_2)S$ coincides with the volume of the eutectic liquid formed as a result of the interaction. It is further assumed that no convection or liquid movement takes place and that the only movement is related with diffusion of the major components in the eutectic melt. Ni is transported by diffusion from Inconel to Zry and Zr by the same reason, from Zry to Inconel. Both diffusion processes are considered as completely independent of each other. The second Fick's law can be applied for Ni and Zr:

$$\frac{\partial C^{Zr}}{\partial t} = D^{Zr} \frac{\partial^2 C^{Zr}}{\partial x^2} \tag{3}$$

$$\frac{\partial C^{Ni}}{\partial t} = D^{Ni} \frac{\partial^2 C^{Ni}}{\partial x^2} \tag{4}$$

Zr and Ni diffusion in solid Inconel and Zry are neglected because, on the one hand, the diffusion coefficients are very small as compared with liquid diffusion coefficients and, on the other hand, this would introduce in the model certain boundary concentrations and diffusion coefficients which are not well known, specially if we consider that diffusion is taking place in the multi-component alloys Inconel and Zry. Moreover, the number of solid phases is influenced by diffusion of the other components present in the melt.

The model also considers that in order to produce the liquefaction of a thickness Δx_2 of Zry it is necessary that a certain quantity of Ni, $\Delta x_2 C_2^{Ni}$, is transported by diffusion from Inconel to Zry in the time step Δt. If C_1^{Ni} and C_2^{Ni} are, respectively, the maximum and the minimum concentrations of Ni in the melt (Figure 5), then:

$$C_2^{Ni} \frac{dx_2}{dt} = \left[-D^{Ni} \frac{\partial C^{Ni}}{\partial x} \right]_{x=x_2} \tag{5}$$

With the same hypothesis for Zr in the eutectic we can write:

$$-C_2^{Zr} \frac{dx_1}{dt} = \left[-D^{Zr} \frac{\partial C^{Zr}}{\partial x} \right]_{x=-x_1} \tag{6}$$

The following equations were obtained from the experimental results:

$$x_1=\sqrt{K_{Exp.}^{Inconel}t} \tag{7}$$

and

$$x_2=\sqrt{K_{Exp.}^{Zircaloy}t} \tag{8}$$

Then

$$\frac{x_1}{x_2}=a \tag{9}$$

with

$$a=\sqrt{\frac{K_{Exp.}^{Inconel}}{K_{Exp.}^{Zircaloy}}} \tag{10}$$

The solutions of eqs.(3) and (4) are:

$$C^{Zr}=A+B\,erf\left(\frac{x}{2\sqrt{D^{Zr}t}}\right) \quad ; \quad C^{Ni}=C+D\,erf\left(\frac{x}{2\sqrt{D^{Ni}t}}\right) \tag{11}$$

With the boundary conditions:

$$C^{Zr}=C_1^{Zr} \quad at\ x=x_2 \quad ; \quad C^{Ni}=C_1^{Ni} \quad at\ x=-x_1 \tag{12}$$

$$C^{Zr}=C_2^{Zr} \quad at\ x=-x_1 \quad ; \quad C^{Ni}=C_2^{Ni} \quad at\ x=x_2 \tag{13}$$

In order that the solutions of eqs.(11) be valid for every time t, we define

$$\gamma_1=\frac{x_1}{2\sqrt{D^{Zr}t}} \quad ; \quad \gamma_2=\frac{x_2}{2\sqrt{D^{Zr}t}} \tag{14}$$

where γ_1 and γ_2 are positive constants. From eq.(9) we have:

$$\gamma_1=a\,\gamma_2 \tag{15}$$

The concentration of Zr in the melt is then:

and that of Ni is:

$$C^{Zr}=C_2^{Zr}-\frac{C_2^{Zr}-C_1^{Zr}}{erf(\gamma_1)+erf(\gamma_2)}\left[erf(\gamma_1)+erf\left(\frac{x}{2\sqrt{D^{Zr}t}}\right)\right] \tag{16}$$

$$C^{Ni}=C_1^{Ni}-\frac{C_1^{Ni}-C_2^{Ni}}{erf(\gamma_1\phi)+erf(\gamma_2\phi)}\left[erf(\gamma_1\phi)+erf\left(\frac{x}{2\sqrt{D^{Ni}t}}\right)\right] \tag{17}$$

where

$$\phi=\sqrt{\frac{D^{Zr}}{D^{Ni}}} \tag{18}$$

If eq.(16) is used to calculate the right side of eq.(6) and dx_1/dt is taken from eq.(14), one obtains:

$$C_2^{Zr}a\gamma_2=\frac{C_1^{Zr}-C_2^{Zr}}{erf(a\gamma_2)+erf(\gamma_2)}\frac{\exp^{-\gamma_2^2a^2}}{\sqrt{\pi}} \tag{19}$$

If C_1^{Zr} and C_2^{Zr} are known it is possible to calculate the value of γ_2 from eq.(19).

From eq.(15) it is possible to determine γ_1. If eq.(17) is used to calculate the right side of eq.(5) and dx_2/dt is determined from eq.(14), one obtains:

$$C_2^{Ni}G=\frac{C_1^{Ni}-C_2^{Ni}}{erf(aG)+erf(G)}\frac{\exp^{-G^2}}{\sqrt{\pi}} \tag{20}$$

with

$$G=\gamma_2\phi \tag{21}$$

If C_1^{Ni} and C_2^{Ni} are known it is possible to calculate the value of G from eq.(20). From eq.(14) and the experimental results in eq.(8) we obtain:

$$4\gamma_2^2D^{Zr} = K_{Exp}^{Zircaloy}(T) \tag{22}$$

From this expression we can calculate D^{Zr} and then, from eq.(18), determine D^{Ni} since ϕ is known from eq.(21).

3.2 Determination of Ni and Zr concentrations at the liquid phase boundaries

With the model described above one can try to interpret the experimental results in the case of the Inconel/Zry interaction without an oxide layer on Zry.

The maximum and minimum concentrations of Ni and Zr in the eutectic are needed for each temperature. The available phase diagram is the binary Ni-Zr. Ni is the major component of Inconel 718 (54wt%Ni) and Zr is the major component of Zry (98.5wt%Zr). Nevertheless, the solidus and liquidus lines in the binary Ni-Zr system and the eutectic temperatures can be very different to those in the Inconel/Zircaloy multi-component system.

In Figure 6 the Ni-Zr phase diagram is represented. The concentrations that can be used for 1000, 1100 and 1200°C for Ni and Zr are indicated by solid points.

In order to determine the concentrations of Ni and Zr at each point of the melt and at the interfaces it is necessary to make certain considerations. The weight percent of Zry and Inconel sum up to 100%. With w^{Zry} we indicate the weight fraction of Zry and with w^{Inc} that of Inconel in the melt. Then:

$$w^{Zry}+w^{Inc}=1 \tag{23}$$

According to the Zr content of Zry, we may approximate $w^{Zry} \approx w^{Zr}$. The case of Inconel is different since Ni represents the 54wt% and the remaining 46wt% is formed by other metals which we shall refer to as "the rest". Starting from eq.(23) we can write:

$$w^{Zr}+w^{Ni}+w^{rest}=1 \tag{24}$$

Here the weight fractions are referred to the total mass of liquid. If, instead, we refer them to the mass formed by Zr and Ni, we have:

$$(w^{Zr}+w^{Ni})(1+\frac{w^{rest}}{w^{Ni}}\cdot\frac{w^{Ni}}{w^{Zr}+w^{Ni}})=1 \tag{25}$$

The fraction w^{rest}/w^{Ni} = 0.46/0.54 is given by the composition of Inconel and the fractions

$$w'^{Ni} = \frac{w^{Ni}}{w^{Ni}+w^{Zr}} \quad ; \quad w'^{Zr} = 1 - w'^{Ni} \tag{26}$$

quantity

$$B = w^{Ni}+w^{Zr} \tag{27}$$

is less than 1 and that it depends, like w'^{Ni}, on the abscissa x under consideration. In particular we calculate B_1 at $-x_1$ and B_2 at x_2 from eq.(25).

$$B_1 = [1+\frac{0.46}{0.54}w'^{Ni}_1]^{-1} \quad ; \quad B_2 = [1+\frac{0.46}{0.54}w'^{Ni}_2]^{-1} \tag{28}$$

With C_0^{Ni} and C_0^{Zr} we designate the Ni and Zr concentrations of the unreacted solids, Inconel and Zry, respectively, measured in g/cm^3. We have:

$$C_0^{Ni} = 0.54\ \delta^{Inc} \quad ; \quad C_0^{Zr} = \delta^{Zry} \tag{29}$$

where $\delta^{Inc}=8.2$g/cm^3 and $\delta^{Zry}=6.5$g/cm^3 represent the densities of the original solid alloys Inconel and Zircaloy, respectively.

The concentrations of Ni and Zr at both interfaces, C_1^{Ni}, C_2^{Ni}, C_1^{Zr} and C_2^{Zr} (Figure 5) are related to the liquid density and to the Ni and Zr fractions in the melt by:

$$\begin{aligned} C_1^{Ni}&=w_1^{Ni}\ \delta^{liq} \quad ; \quad C_2^{Ni}=w_2^{Ni}\ \delta^{liq} \\ C_2^{Zr}&=w_1^{Zr}\ \delta^{liq} \quad ; \quad C_1^{Zr}=w_2^{Zr}\ \delta^{liq} \end{aligned} \tag{30}$$

The assumption of a constant liquid density, i.e. independent of the abscissa x, is implied in eqs.(30).

The determination of this density is obtained from the condition of conservation of Ni and Zr mass. The concentration profiles of Ni and Zr are functions of x and t but, given that they are determined by their diffusion in the liquid, it is reasonable to assume that these profiles rapidly approach a straight line. This means that:

$$\frac{1}{2}(C_1^{Ni}+C_2^{Ni})(x_1+x_2) = C_0^{Ni}x_2$$

$$\frac{1}{2}(C_1^{Zr}+C_2^{Zr})(x_1+x_2) = C_0^{Zr}x_2$$

The condition of conservation of the total volume is also implied. This means that the volume initially occupied by Inconel and Zircaloy is after reaction occupied by the melt. In other words, this implies the assumption that no expansion is produced due to liquid formation from the solid. By addition we obtain:

$$\frac{1}{2}(x_1+x_2)(C_1^{Ni}+C_2^{Ni}+C_1^{Zr}+C_2^{Zr}) = (C_0^{Ni}x_1 + C_0^{Zr}x_2)$$

From eqs.(27) and (30) we have: $C_1^{Ni}+C_2^{Zr}=B_1\delta^{liq}$ and $C_2^{Ni}+C_1^{Zr}=B_2\delta^{liq}$, from where:

$$\delta^{liq} = \frac{2}{(B_1+B_2)}[C_0^{Ni}(\frac{a}{1+a}) + C_0^{Zr}(\frac{1}{1+a})] \qquad (31)$$

In order to determine the concentrations of Ni and Zr at both interfaces using the values read from the binary Ni-Zr phase diagram (w'^{Ni} and $w'^{Zr}=1-w'^{Ni}$), eqs.(30) must be slightly modified, using the definitions of w' and B given in eqs.(26) and (27). They become:

$$C_1^{Ni}=B_1w'^{Ni}_1\ \delta^{liq} \quad ; \quad C_2^{Ni}=B_2w'^{Ni}_2\ \delta^{liq}$$
$$C_2^{Zr}=B_1w'^{Zr}_1\ \delta^{liq} \quad ; \quad C_1^{Zr}=B_2w'^{Zr}_2\ \delta^{liq} \qquad (32)$$

In summary, from the experimental values of the interfaces positions, the parameter a can be determined for the corresponding temperatures. With the binary Ni-Zr phase diagram and eqs. (28) the parameters B_1 and B_2 are determined. These values along with the densities of solid Zry and Inconel allow us to calculate the density of the melt, δ^{liq}, with the aid of eq.(29) and (31). By means of eqs.(32) the Ni and Zr concentrations at both interfaces are determined. The calculation proceeds as described in 3.1 to determine the values of D^{Zr} and D^{Ni}.

The solid/solid interaction model is applied now to analyze the case with an oxide layer on the Zry surface.

3.3 Influence of an oxide layer on the Zircaloy surface

In order to understand the influence of an oxide layer on the Zry surface, the model described above was used with some changes. Without an initial oxide layer the kinetics results plotted as x^2 versus t are straight lines through the origin. This is not true when an oxide layer is present on Zry, in which case a delay time t_0 appears. For this reason the slopes of the lines x^2/t, like those shown in Figures 2a and 2b, were used to represent the kinetic data as $\ln\{x^2/(t-t_0)\}$ versus the reciprocal of the absolute temperature, as in Figures 3 and 4. Only the slopes of the lines are considered in this section. The delay time t_0 will be discussed later on. Eqs.(7) and (8) must be replaced by

$$x_1=\sqrt{K_{Exp.}^{Inconel}(T,X,t_o)t}$$

and

$$x_2=\sqrt{K_{Exp.}^{Zircaloy}(T,X,t_o)t}$$

and eq.(10) by

$$a = \sqrt{\frac{K_{Exp.}^{Inconel}(T,X,t_o)}{K_{Exp.}^{Zircaloy}(T,X,t_o)}} \qquad (33)$$

where X is the initial ZrO_2 layer thickness.

3.4 The delay time problem; the DISOL code

As a first approximation the delay time t_0 can be related to the time needed by Zry to chemically dissolve the oxide layer by formation of α-Zr(O).

The DISOL code is designed to describe the evolution of the ZrO_2, α- and ß-Zr layers, which distribution is shown in Figure 7, produced during high temperature oxidation of Zr. It also describes the dissolution of the oxide layer when the oxygen supply is interrupted. The ß-phase layer thickness also decreases until it disappears and consequently, after a sufficiently long heat treatment, the α-phase occupies the whole thickness of the sample. The calculation code describes all these processes until the oxygen concentration is homogeneous in the considered specimen.

The model assumes that the process is controlled by oxygen diffusion and that it can be described by a one-dimensional space variable. The second Fick's law is applied to the different phases.

$$\frac{\partial C}{\partial t} = D\frac{\partial^2 C}{\partial x^2} - \frac{\partial}{\partial x}(vC) \tag{34}$$

The first order term is effectively present only when the diffusion equation is applied to the oxide. A rigid displacement of this phase appears due to the lattice expansion produced at the oxide/α-Zr interface, where the oxide is generated (Figure 8.a). The disappearance (or formation) of a thickness $d\xi$ of α-Zr during oxide growth (or during oxide dissolution) is related with the formation (or disappearance) of a thickness $fd\xi$ of oxide, where f takes the value 1.56 for Zr [7]. Consequently, the oxide moves at a speed $v=-(f-1)d\xi/dt$.

As for the Stefan problem, we must look at a given interface at ξ, as in Figure 8b, and consider that the difference between the incoming and outcoming fluxes gives origin to the interface movement.

$$\Delta C\frac{d\xi}{dt} = J_{in} - J_{out} \tag{35}$$

where the flux J takes in planar coordinates the form:

$$J = -D\frac{\partial C}{\partial x} + vC \tag{36}$$

During the first step of the experiment the sample is placed in an oxidizing atmosphere at the constant temperature T_i. In this period oxide layers grow on both faces of the sample. Underlying α-Zr regions and a central ß-Zr region are also generated. Although the real geometry of the sample is cylindrical, for simplicity and as a first approach we have solved the equations in planar coordinates. The approximation is justified by the fact that the thicknesses of the phases are small as compared with the insert radii. In this case symmetry allows us to solve the problem in one half of the sample. The information about the experimental conditions is given to the equations through the boundary conditions. These are, during the oxide growth, of constant oxygen concentrations at the gas/oxide, oxide/α-Zr and α-Zr/ß-Zr interfaces. Instead, at the middle of the sample the condition of no oxygen flux (oxygen concentration gradient equal zero) is imposed.

While the oxide layer and the α-phase grow, the ß-phase thickness decreases. Once a given oxide layer thickness is reached, the temperature is abruptly varied to T_d. During this second step no oxygen enters into the sample from the environment and the oxide dissolution starts, for which simulation the boundary condition at the entrance face is changed to oxygen concentration gradient equal zero. The ß-phase, at the same time, continues to decrease. Its disappearance can take place before or after that of the oxide, depending on both temperatures T_i and T_d and on the initial wall thickness of Zry. The final step consists of the oxygen homogenization in the single, α-phase.

Equations (36), one for each phase, admit an analytical solution when a semi-infinite system is considered. In this case the oxygen concentration profiles are described by error functions and the interfaces movement obey parabolic rate laws. This is a good representation of the real solution in the sample as long as it may be considered as semi-infinite, i.e. as long as the oxygen concentration at the middle of the sample does not differ significantly from that of the as-received Zry. Consequently, the initial, analytical solution must be calculated at a given time t_1 for which this condition is verified. Henceforth, the numerical method is used.

The finite differences method, which was used in this work, requires a space and time grid. Due to the kinetics of this experiment, phases of markedly different thicknesses appear. The choice of a single space grid for all the phases which could render a reasonable number of points in every phase becomes impracticable. For this reason we have preferred to develop a calculation method which allows for the definition of different space grids in each phase. Moreover, the grids would accompany the growth and decrease of the phases thickness by being able to interpolate new points between two net points when the phase under consideration becomes thin and the number of net points is too low to define the concentration profile properly. It must be also capable of increasing the space grid width when the phase thickens and the number of net points becomes too high. But the major difficulty arising from this ability of the calculation method lies in the impossibility of describing each phase with a number of equidistant points. In fact uniform spacing between nodes can be maintained within each phase but not at the phase boundaries. This idea was first proposed in [8] and more recently used in [6]. When the space and time partial derivatives of concentrations are replaced in eq.(36) by its finite differences approximation, using a centered scheme,

$$\left.\frac{\partial C}{\partial t}\right|_{i}^{k} = \frac{C_i^{k+1}-C_i^{k}}{\Delta t}$$

$$\left.\frac{\partial C}{\partial x}\right|_{i}^{k+1} = \frac{C_{i+1}^{k+1}-C_{i-1}^{k+1}}{2\,\Delta x} \qquad \textbf{(39)}$$

$$\left.\frac{\partial^2 C}{\partial x^2}\right|_{i}^{k+1} = \frac{C_{i+1}^{k+1}-2C_i^{k+1}+C_{i-1}^{k+1}}{2\,\Delta x^2}$$

the following equation is obtained:

$$C_i^{k} = -(R+S)C_{i-1}^{k+1} + (1+2R)C_i^{k+1} - (R-S)C_{i+1}^{k+1} \qquad \textbf{(40)}$$

with R and S defined as

$$R=\frac{D\Delta t}{\Delta x^2} \quad \text{and} \quad S=v\frac{\Delta t}{2\,\Delta x}$$

The subscripts stand for the space level and the superscripts for the time level.
The expression (40) shows that the concentrations at the different nodes are not independent of each other. The solution at the nodes of the net at the time level t^{k+1} is calculated from the solution at the time t^k. When eq.(40) is applied to every net node between the domain edges of the partial differential equation, a system of linear equations is obtained which solution yields the values of the unknown concentrations at any given time and space level.

A different system of equations has to be constructed for each phase (which differ in the values of the diffusion coefficient of oxygen, D, and of the grid spacing, Δx), according to the number of phases present at the instant under consideration. These systems of equations are, however, connected by a common value of Δt which is calculated in such a way that during the time interval Δt anyone of the interfaces reaches the nearest space node.

The calculation procedure is as follows: given that the numerical method requires of a concentration profile to start the calculation with, an initial solution of the oxygen diffusion problem in the three phases system is analytically calculated at a given time t_1 chosen with the criterion of semi-infinite system stated above. The oxygen concentration at the interfaces and the diffusion coefficient of oxygen in all the phases must be previously calculated at the temperature T_i. The numerical calculation proceedes as described in [6].

The system of M linear equations with M unknowns can be written in the matrix form:

$$\begin{vmatrix} b_1 & c_1 & 0 & \cdot & \cdot & \cdot & \cdot & \cdot & \cdot & \cdot & \cdot \\ a_2 & b_2 & c_2 & 0 & \cdot & \cdot & \cdot & \cdot & \cdot & \cdot & \cdot \\ 0 & a_3 & b_3 & c_3 & 0 & \cdot & \cdot & \cdot & \cdot & \cdot & \cdot \\ \cdot & \cdot & \cdot & \cdot & \cdot & \cdot & \cdot & \cdot & \cdot & \cdot & \cdot \\ \cdot & \cdot & \cdot & \cdot & \cdot & \cdot & \cdot & 0 & a_{M-1} & b_{M-1} & c_{M-1} \\ \cdot & \cdot & \cdot & \cdot & \cdot & \cdot & \cdot & \cdot & 0 & a_M & b_M \end{vmatrix} \begin{vmatrix} C_1 \\ C_2 \\ C_3 \\ \cdot \\ C_{M-1} \\ C_M \end{vmatrix}^{k+1} = \begin{vmatrix} C_1+lb \\ C_2 \\ C_3 \\ \cdot \\ C_{M-1} \\ C_M+rb \end{vmatrix}^{k}$$

where the matrix elements a,b and c, in the case of constant concentrations at both boundaries (constant C_A and C_B), are given by:

$a_1=0$

$b_1=1+2R(1-pS/R)/(1+p)$

$c_1=-2R\{1-(1+p)S/R\}/(2+p)$

$a_i=-R-S$

$b_i=1+2R$ $\qquad$ $i=2,\ldots,M-2$

$c_i=-R+S$

$a_{M-1}=-2R\{1+(1+q)S/R\}/(2+q)$

$b_{M-1}=1+2R(1+qS/R)/(1+q)$

$c_{M-1}=0$

lb (left boundary) and rb (right boundary) are:

If the boundary condition is of oxygen flux equal zero at the right edge of the phase, which

$$lb=\frac{2RC_A(1+S/R)}{(1+p)(2+p)} \qquad rb=\frac{2RC_B(1-S/R)}{(1+q)(2+q)}$$

is the case of the ß-phase, the above definitions must be modified in:

$$\begin{aligned} a_{M-1} &= -2R[1+2(1+q)S/R]/(3+2q) \\ b_{M-1} &= 1+2R[1+2(1+q)S/R]/(3+2q) \\ rb &= 0 \end{aligned}$$

If, on the contrary, the boundary condition is of oxygen flux equal zero at the left edge of the phase, which is the case of the oxide during its dissolution, they change to:

$$\begin{aligned} b_1 &= 1+2R[1-2(1+p)S/R]/(3+2p) \\ c_1 &= -2R[1-2(1+p)S/R]/(3+2p) \\ lb &= 0 \end{aligned}$$

A tridiagonal system like this one is stable if the matrix is diagonal dominant, i.e., if $|b| > |a| + |c|$. This condition is fulfilled in our problem, so that standard equation solutions for tri-diagonal matrixes can be used.

Starting from the concentration profile at the time level k, the solution at the time level k+1 is attained by inversion of the matrix (one for each phase). This procedure is quite simple due to the sparsity of the matrix elements and demands very little calculation time.

4. RESULTS

4.1 The solid/solid interaction model applied to the Inconel/Zry system

The calculation procedure described in 3.1, 3.2 and 3.3 yields the values of the diffusion coefficients of Zr and Ni in the eutectic formed due to the interaction between Inconel and Zry with and without an initial oxide layer. The points shown in the Arrhenius type plots of Figures 9a and 9b represent the values of the diffusion coefficients obtained with this calculation. The lines are the least square fit which are expressed by:

$$
\begin{aligned}
D^{Zr} &= 9.716x10^{-3}\exp(-71631/RT) \quad for\ X=0\mu m\\
D^{Zr} &= 1.357x10^{3}\exp(-212913/RT) \quad for\ X=20\mu m\\
D^{Zr} &= 1.246x10^{9}\exp(-390400/RT) \quad for\ X=45\mu m\\
D^{Zr} &= 3.038x10^{-4}\exp(-35473/RT) \quad for\ X=100\mu m
\end{aligned}
\tag{41}
$$

$$
\begin{aligned}
D^{Ni} &= 2.316x10^{-2}\exp(-80316/RT) \quad for\ X=0\mu m\\
D^{Ni} &= 0.1473\exp(-105031/RT) \quad for\ X=20\mu m\\
D^{Ni} &= 2.075x10^{4}\exp(-261550/RT) \quad for\ X=45\mu m\\
D^{Ni} &= 1.077x10^{-5}\exp(-6582.5/RT) \quad for\ X=100\mu m
\end{aligned}
\tag{42}
$$

where the activation energies are measured in J/mol, the gas constant R is 8.314 J/mol K, T in K, D^{Zr} and D^{Ni} in cm^2/s and X is the initial oxide layer thickness. Particularly, when no initial oxide layer is present the activation energies and frequency factors of D^{Zr} and D^{Ni} in the eutectic obtained with the code are reasonable for liquid diffusion processes.

Both diffusion coefficients show similar values, specially for 0, 20 and 100μm; for 45μm they have higher activation energies and higher frequency factors.

In order that these diffusion coefficients may be used by a SFD code, a correlation for other oxide layer thicknesses is necessary. But, due to the complicate behavior of the diffusion coefficients evidenced in Figure 9 it is easier to correlate the frequency factor and the activation energy of each diffusion coefficient separately. They are shown in Figures 10a and 10b and may be represented by the expressions:

$$\ln D_0^{Zr} = \begin{cases} 5675.9X - 4.4573 & \mathit{for}\ 0 \leq X \leq 45\mu m \\ -5280.4X + 44.705 & \mathit{for}\ 45\mu m \leq X \leq 100\mu m \end{cases}$$

$$\ln D_0^{Ni} = \begin{cases} 3115.1X - 5.3293 & \mathit{for}\ 0 \leq X \leq 45\mu m \\ -3659.5X + 25.156 & \mathit{for} 45\mu m \leq X \leq 100\mu m \end{cases}$$

$$Q^{Zr} = \begin{cases} 7.0844x10^7 X + 71486 & \mathit{for}\ 0 \leq X \leq 45\mu m \\ -6.4511x10^7 X + 680584 & \mathit{for}\ 45\mu m \leq X \leq 100\mu m \end{cases}$$

$$Q^{Ni} = \begin{cases} 4.1119x10^7 X + 59722 & \mathit{for}\ 0 \leq X \leq 45\mu m \\ -4.3362x10^7 X + 440203 & \mathit{for}\ 45\mu m \leq X \leq 100\mu m \end{cases}$$

4.2 The delay time solution

The experimental and calculated values of the delay time t_o are represented in an Arrhenius type plot in Figure 11. The nearly linear relationship linking the experimental points suggests the assumption that the delay time t_o is due to the dissolution of the oxide layer, which is a thermally activated process.

In order to analyze the experimental results we use the DISOL code to simulate the Zry oxidation at a given temperature up to a given oxide layer thickness and then the oxide layer dissolution at the same temperature. In Figure 12 the case of an oxide layer 45μm thick generated and dissolved at 1000°C is represented. Here, an external layer of α-Zr and an underlying layer of ß-Zr remain in the sample. The DISOL code gives the time to generate the oxide layer and to dissolve it.

In Figure 13 the interfaces positions are plotted as functions of the square root of time for the same example as in Figure 12. The oxide layer grows in the oxidation period up to $\sqrt{t}=41.6\sqrt{s}$ (Figure 12). In the dissolution period the oxide layer thickness is reduced up to its complete disappearance, at $\sqrt{t}=235.8\sqrt{s}$. The total oxide layer size is also plotted in the same figure, fixing the coordinate origin at the external surface, in order to compare with the experimental results indicated with the square points. It may be seen that the results of the DISOL calculations are in good agreement with the experimental results.

In the temperature range of the experiments and for different oxide layers of 10, 20, 45 and 100μm the DISOL code was run in order to obtain the dissolution time t_0. The results corresponding to the same initial oxide layer thickness may be well correlated by a straight line. Moreover, the lines for different oxide thicknesses have approximately the same slope and are shown by the full lines of Figure 11. We use an average slope of 26596sK to represent the results of DISOL. The intercepts of these lines (obtained from Figure 11 for 1/T=0) verify with the oxide thickness a nearly parabolic law. We found that the expression $2.53X^2$, where X is the initial oxide layer thickness, gives an adequate fitting. In summary, the results of DISOL are represented by:

$$t_0=2.53\,X^2\,e^{26596/T} \tag{44}$$

Comparison between the experimental points and the lines calculated with DISOL (Figure 11) indicates that the fitting is good only for the 10μm oxide thickness. The dissagreement observed for the higher thicknesses indicate that another mechanism, besides the oxide dissolution, is also operating during the chemical attack between Inconel and Zircaloy, which accelerates the process. We can reasonably assume that high temperature fast diffusion of Ni and Zr through the oxide layer is also taking place during the oxide dissolution. This hypothesis is corroborated by experimental observations where the oxide layer appears sandwiched between two eutectic liquids.

hypothesis is corroborated by experimental observations where the oxide layer appears sandwiched between two eutectic liquids.

The experimental points shown in Figure 11 can be fitted by least squares lines which expressions are:

$$\begin{aligned} t_0 &= 2.661x10^{-8}\ e^{268438/RT} \quad for \quad X = 10\mu m \\ t_0 &= 7.700x10^{-17}\ e^{524339/RT} \quad for \quad X = 20\mu m \\ t_0 &= 6.762x10^{-15}\ e^{475227/RT} \quad for \quad X = 45\mu m \\ t_0 &= 1.875x10^{-9}\ e^{329218/RT} \quad for \quad X = 100\mu m \end{aligned} \tag{46}$$

where the constant R is 8.314 J/mol K, T in K, t_o in s and X is the initial oxide layer thicknesses.

4.3 Verification of the results

The calculation procedure described above allows us, starting from the reaction rate constants for Zircaloy and Inconel, to determine the diffusion coefficients of Zr and Ni in the eutectic. In order to verify the correctness of these calculations, the reverse problem was solved. This means that the equation systems (3-22) were again used but in this case the diffusion coefficients given in (41) and (42) were entered as data and the reaction rate constants $K^{Zircaloy}$ and $K^{Inconel}$ were calculated. These values along with those for t_0 obtained from (44) lead us to the determination of the reaction zone thickness, x, as a function of time. An example of this verification is shown in Figure 14a and 14b where x^2 is plotted as a function of the annealing time for the temperature of 1100°C. The points represent the experimental values already shown in Figures 2a and 2b. It may be seen that the fit is reasonably good, specially if we take into account the large experimental error.

5. DISCUSSION

The model of solid/solid interaction that produces an eutectic, seems to be a good tool to interpret the experimental results and obtain diffusion coefficients for Ni and Zr in the eutectic liquid, in good agreement with the diffusion coefficients in liquids. The results we obtain here can be used in SFD numerical codes to predict the reaction layer thicknesses either in isothermal scenarios or during temperature transients.

6. CONCLUSIONS

The chemical interaction between Inconel and Zircaloy can be described by parabolic rate laws. An Arrhenius correlation has been developed for the Zry and Inconel attack at different temperatures and for different initial oxide layers thicknesses on Zircaloy.

Layers of ZrO_2 on Zircaloy delay the onset of chemical interaction and shift the liquefaction of components to higher temperatures. This delay time may be due either to the dissolution of the ZrO_2 layer, which is described by the DISOL code, or to fast diffusion of Ni and Zr through the oxide layer,so that the interaction occurs at the oxide/oxygen stabilized zirconium interface.

The solid/solid chemical interaction model is able to describe the Inconel/Zircaloy interaction at high temperatures and gives the diffusion coefficients of Ni and Zr in the eutectic liquid as functions of temperature. It also describes the Inconel/ZrO_2/ Zircaloy interaction and gives the effective diffusion coefficients which include the effect of temperature and of the initial oxide layer thickness. A correlation was found for D^{Zr} and D^{Ni} as functions of the oxide layer thickness and of temperature.

References

[1] S. Hagen and P.Hofmann, Physical and Chemical Behavior of LWR Fuel Elements up to very High Temperatures, KfK Report 4104(1987).

[2] S.Hagen, P.Hofmann, G.Schanz and L.Sepold, Interaction in Zircaloy/UO_2 Fuel Rod Bundles with Inconel Spacers at Temperatures above 1200 °C; Rest Result of the Experiments CORA-2 and CORA-3, KfK Report 4378(1990).

[3] P.Hofmann and M.Markiewicz, Chemical Behavior of (Ag,In,Cd) absorber rods in severe LWR accidents, KfK report 4670 (1990)

[4] P.Hofmann and M.Markiewicz, Chemical interactions between Inconel spacer grids and Zircaloy fuel rod cladding beyond 1000 °C,KfK Report 4729, in preparation

[5] R.Piotrkowski, A.Denis, J.Kovacs and E.A.García "The validity of the parabolic rate constant during temperature transients". To be published.

[6] A.Denis and E.A.García, J.Nucl.Mater. 185(1991)96-113

[7] A.Denis,E.A.García,J.Nucl.Mater.96(1981)127-140

[8] A.Denis,E.A.García,J.Nucl.Mater.114(1983)75-84

FIGURE CAPTIONS

Figure 1: Chemical interactions between Zircaloy-4 and Inconel 718 at different temperatures; influence of a thin ZrO_2 layer on the reaction behavior (right row).

Figure 2 a: Reacted Zircaloy thickness in the Zircaloy/ Inconel 718 system versus time for different initial oxide layer thicknesses. The presence of oxide layers delays the chemical interaction with Zircaloy.

Figure 2 b: Idem Figure 2 a but on the Inconel side.

Figure 3: Zircaloy consuption rate for the Zircaloy/Inconel 718 system. The presence of oxide layers results in lower rates of attack and shifts the complete liquefaction of the specimens to higher temperatures.

Figure 4: Idem Figure 3 but on the Inconel side.

Figure 5: Schematic representation of the Ni and Zr concentration profiles for $t > t_0$. Δx_1 and Δx_2 are the Inconel and Zircaloy dissolved thickness in the next Δt.

Figure 6: Ni-Zr phase diagram with the maximum and minimum concentrations in the eutectic.

Figure 7: Oxygen concentration profile during oxidation or oxide dissolution. Initially all the interfaces coincide at ξ_0. As the oxidation progresses, the interfaces ξ_2 and ξ_3 displace to the right while ξ_1 moves to the left due to the oxide expansion. The reverse motion occurs during dissolution.

Figure 8 a: Due to oxygen diffusion a layer $d\xi$ of α-Zr transforms to ZrO_2. The different density of Zr atoms between both phases is responsible for the expansion and consequent displacement of the oxide as a whole. Something similar happens during the oxide dissolution.

Figure 8 b: The flux of diffusing substance arriving at any interface, J_{in}, is distributed among the flux entering the next phase J_{out} and that necessary to produce the phase change $\Delta C \, d\xi/dt$.

Figure 9 a: Effective diffusion coefficients of Zr in the eutectic for oxide layers of 0, 20, 45 and 100μm.

Figure 9 b: Effective diffusion coefficients of Ni in the eutectic for oxide layers of 0, 20, 45 and 100μm.

Figure 10 a: Frequency factors of Zr and Ni diffusion, D_0^{Zr} and D_0^{Ni}, for different oxide layer thicknesses.

Figure 10 b: Activation energies of Zr and Ni diffusion, Q^{Zr} and Q^{Ni}, for different oxide layer thicknesses.

Figure 11: Experimental and calculated results of the delay time for Zircaloy/Inconel interaction as a function of the reciprocal of absolute temperature.

Figure 12: DISOL calculations before (full line) and after (dotted line) ZrO_2 dissolution.

Figure 13: Formation and dissapearance of the ZrO_2 layer. Comparison between DISOL calculations and experimental results at 1000°C.

Figure 14 a: Comparison between calculated (full lines) and experimental (points) reacted Zircaloy thickness for the chemical interaction at 1100°C.

Figure 14 b: Idem Figure 14 a but on the Inconel side.

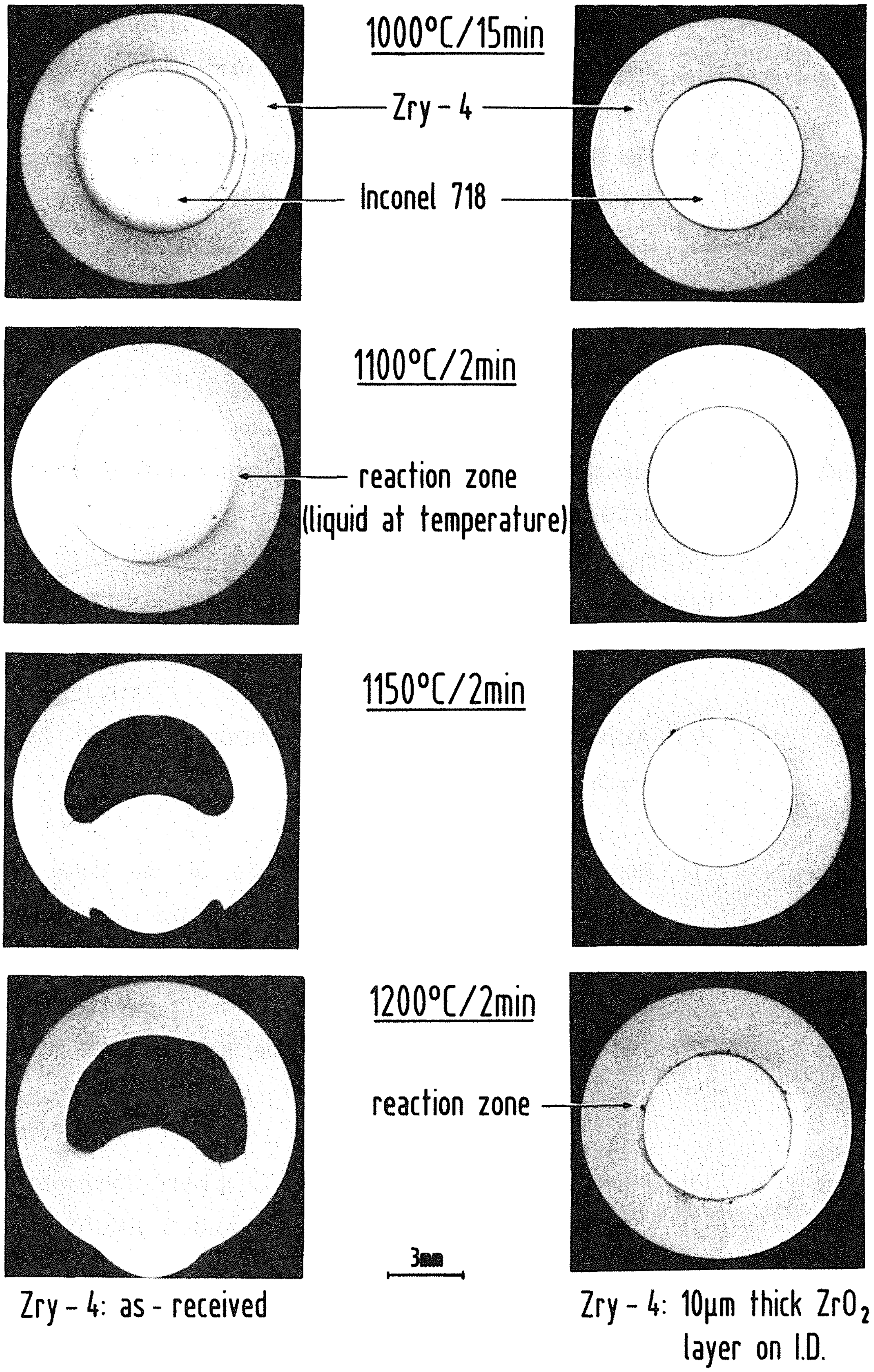

Figure 1: Chemical interactions between Zircaloy-4 and Inconel 718 at different temperatures; influence of a thin ZrO_2 layer on the reaction behavior (right row).

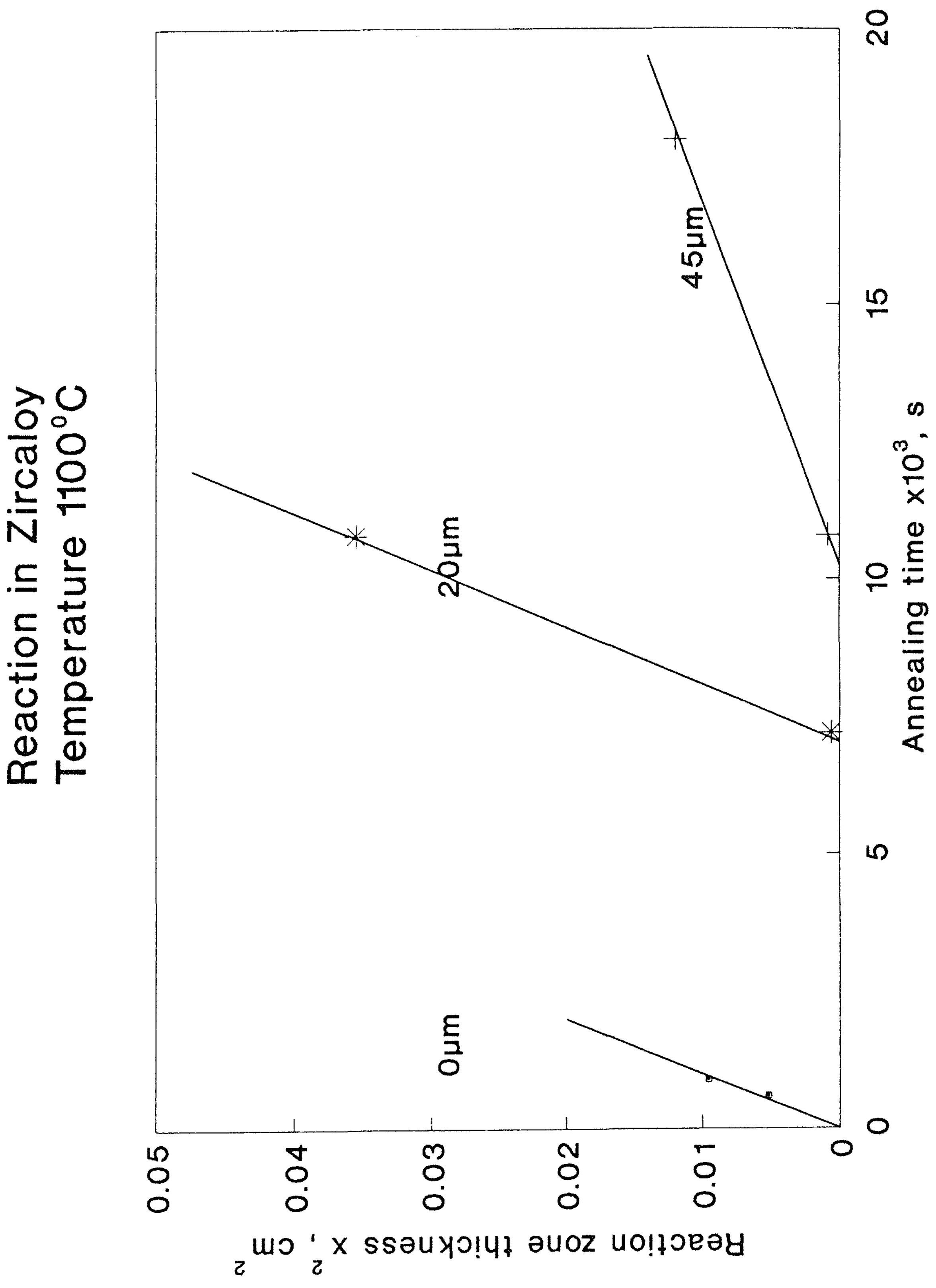

Figure 2 a: Reacted Zircaloy thickness in the Zircaloy/ Inconel 718 system versus time for different initial oxide layer thicknesses. The presence of oxide layers delays the chemical interaction with Zircaloy.

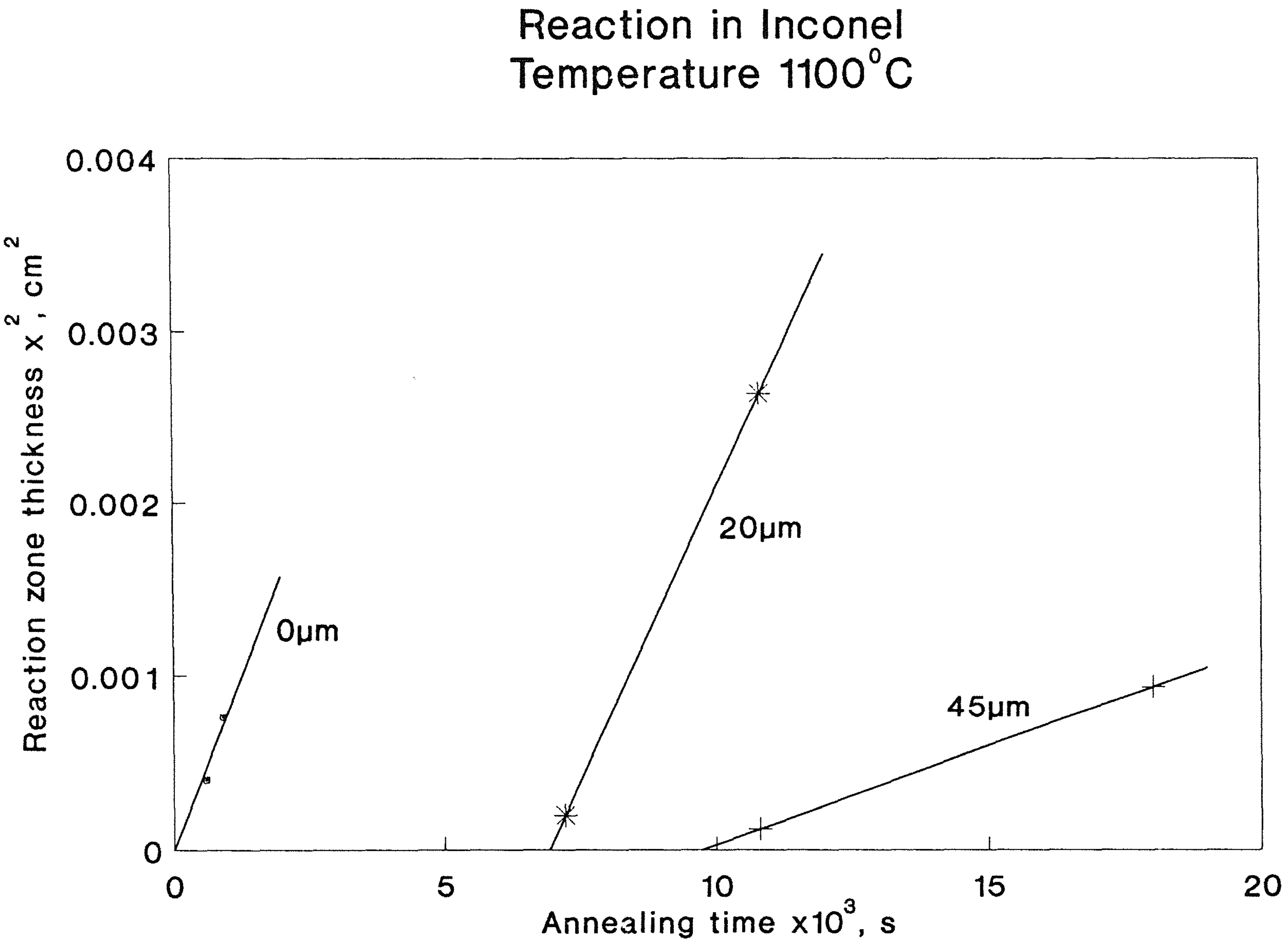

Figure 2 b: Idem Figure 2 a but on the Inconel side.

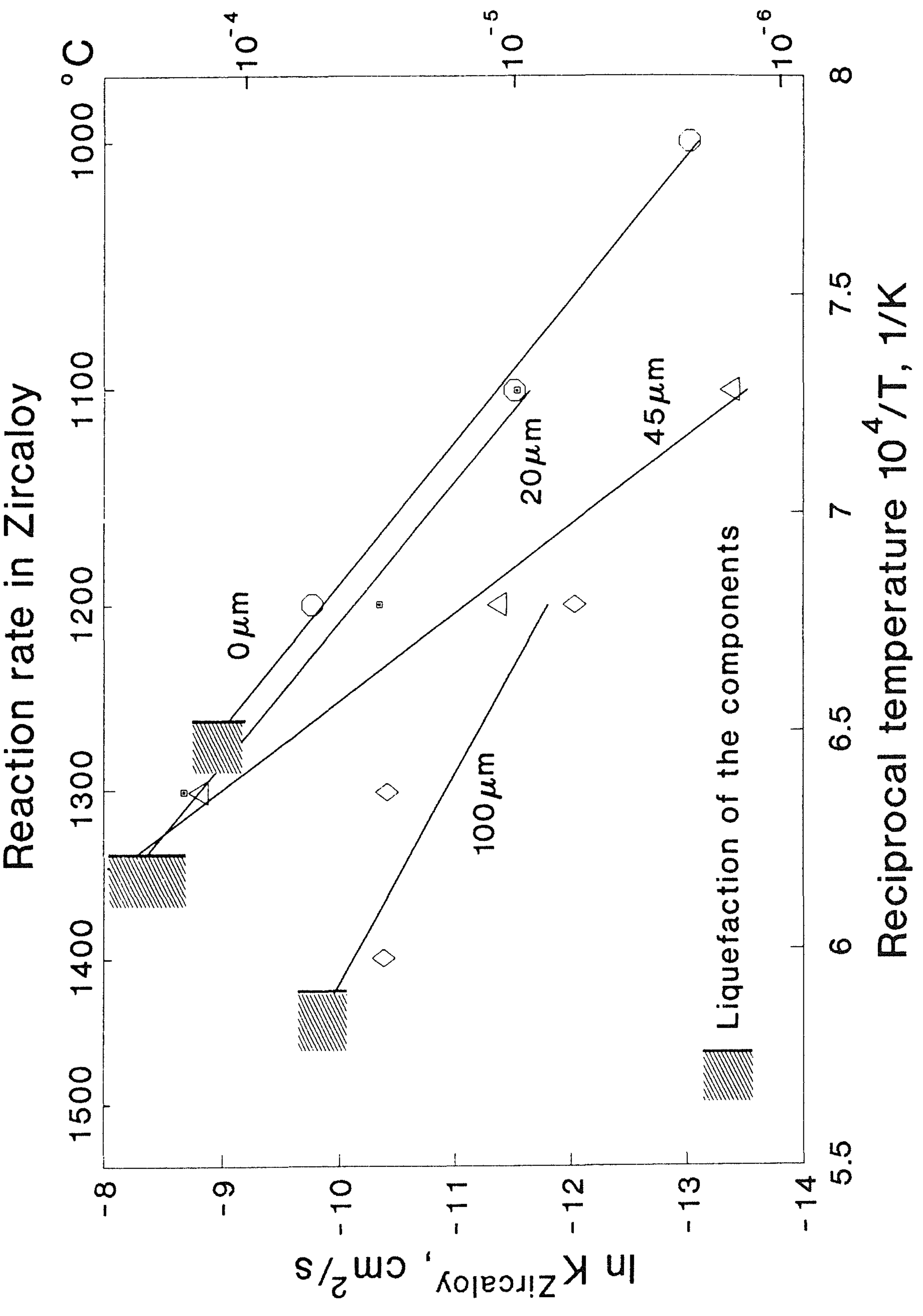

Figure 3: Zircaloy consuption rate for the Zircaloy/Inconel 718 system. The presence of oxide layers results in lower rates of attack and shifts the complete liquefaction of the specimens to higher temperatures.

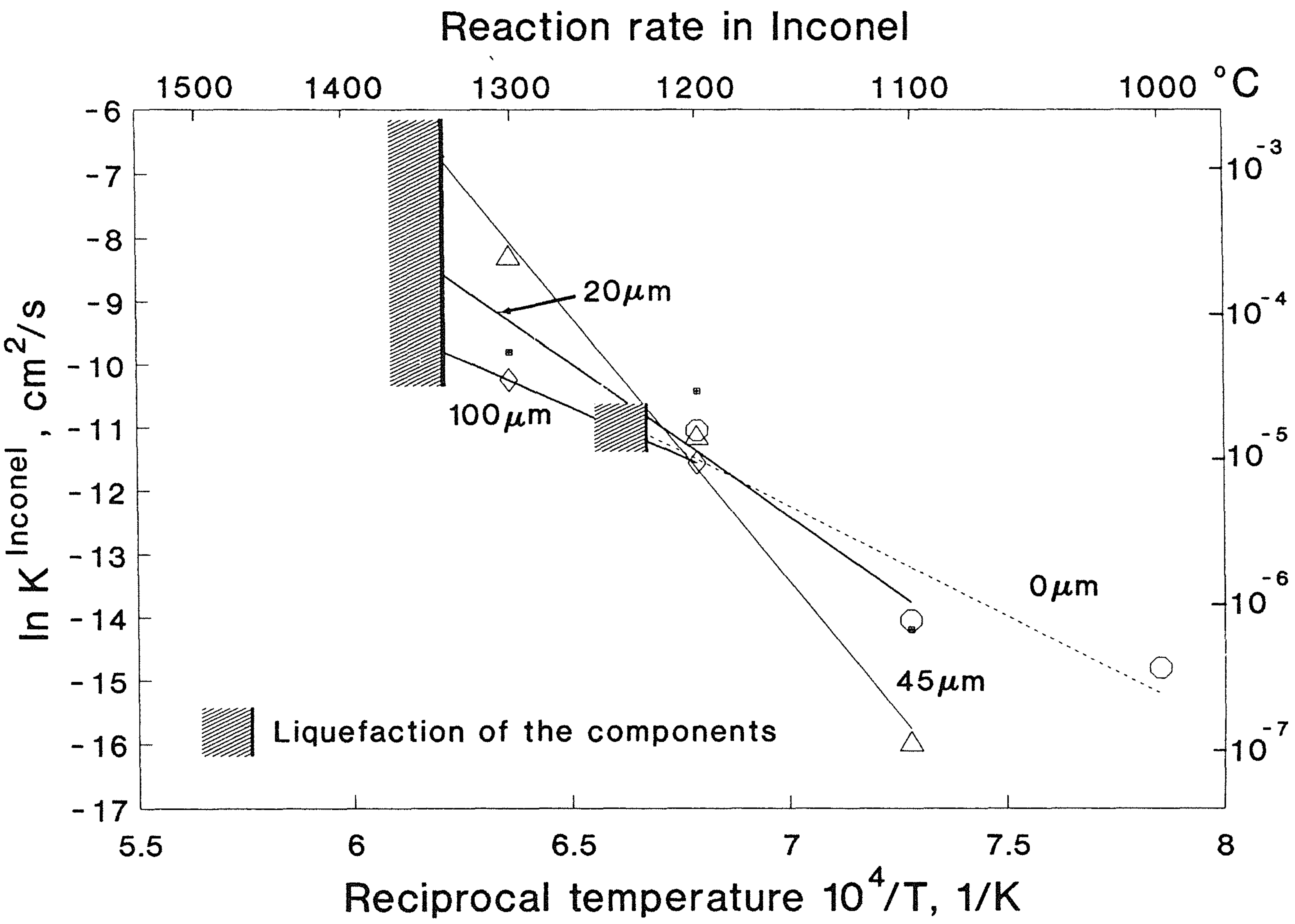

Figure 4: Idem Figure 3 but on the Inconel side.

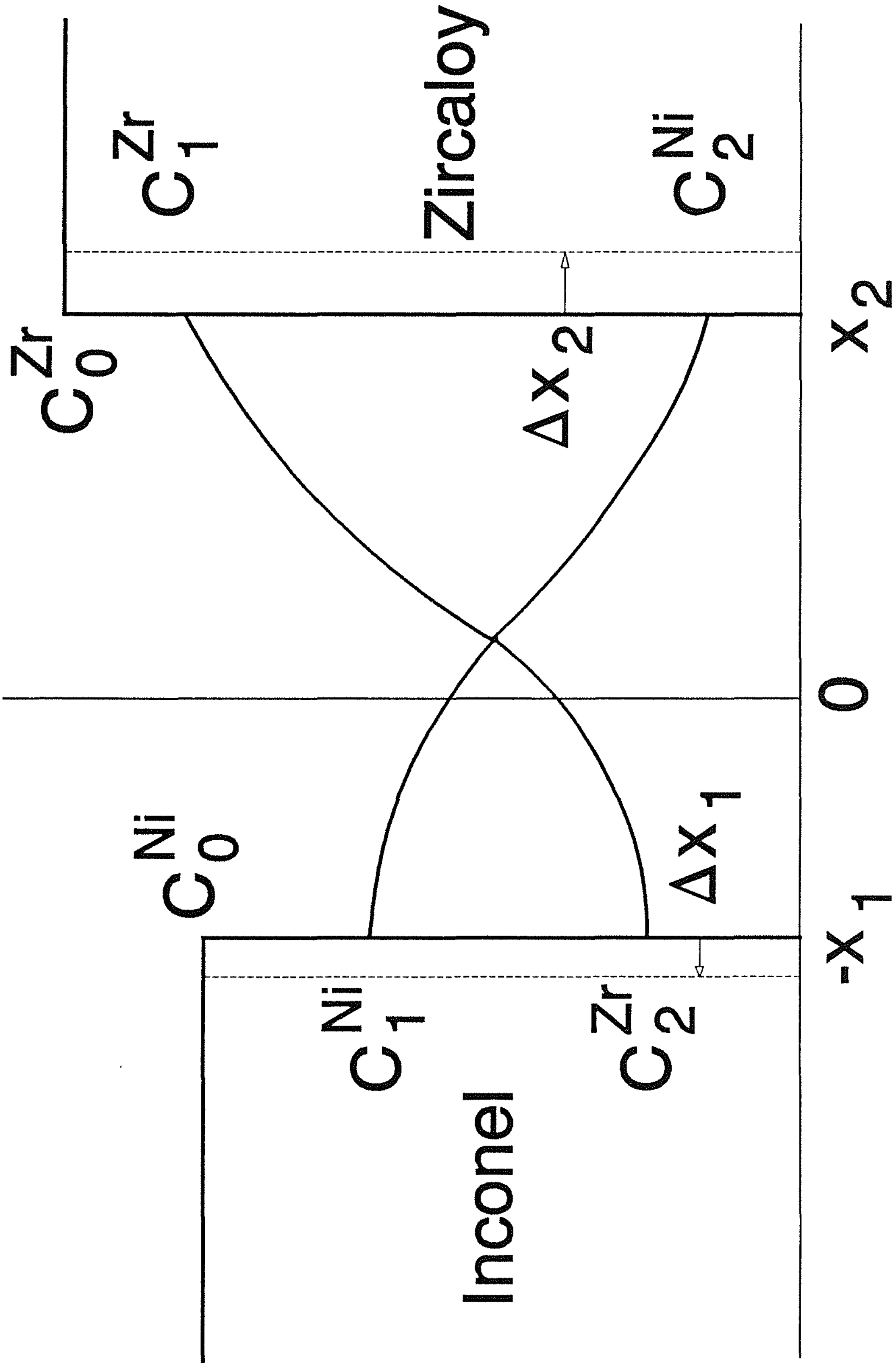

Figure 5: Schematic representation of the Ni and Zr concentration profiles for $t > t_0$. Δx_1 and Δx_2 are the Inconel and Zircaloy dissolved thickness in the next Δt.

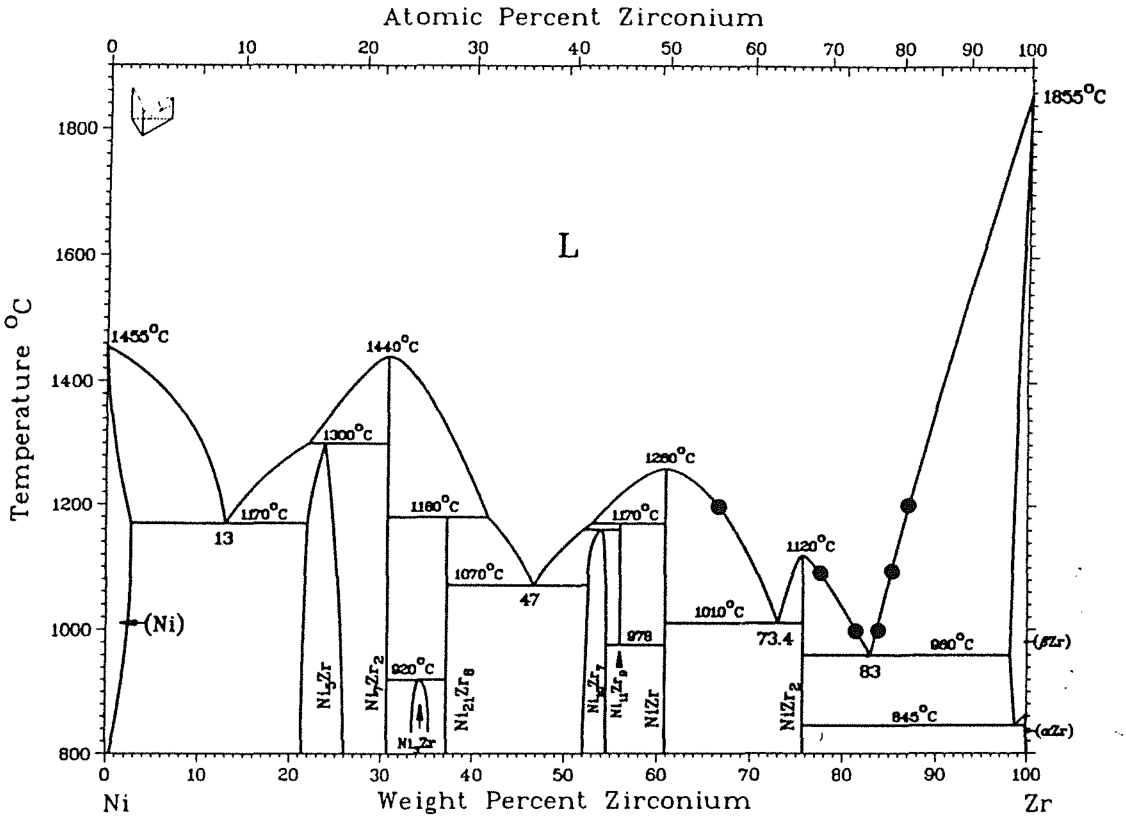

Figure 6: Ni-Zr phase diagram with the maximum and minimum concentrations in the eutectic.

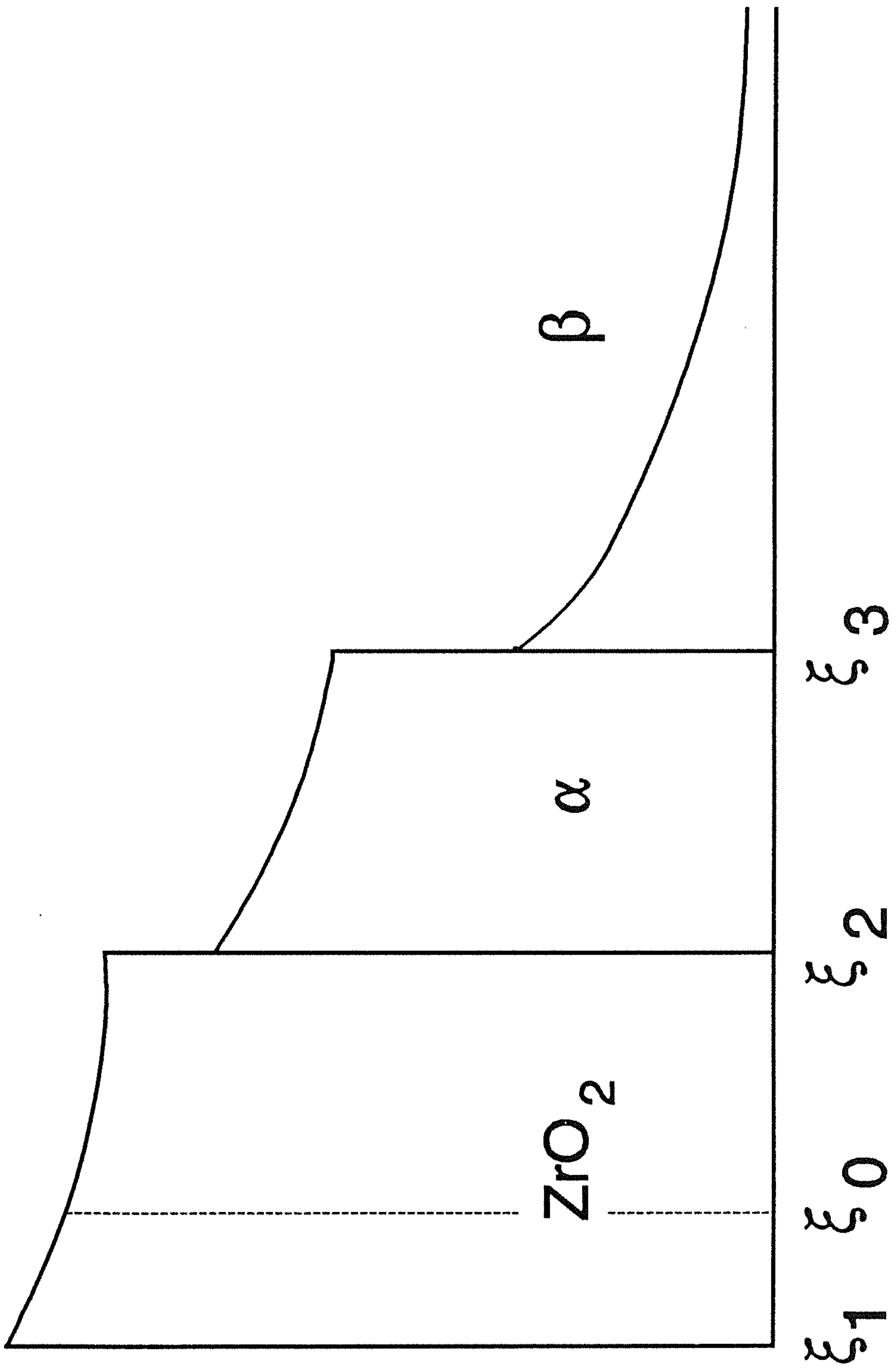

Figure 7: Oxygen concentration profile during oxidation or oxide dissolution. Initially all the interfaces coincide at ξ_0. As the oxidation progresses, the interfaces ξ_2 and ξ_3 displace to the right while ξ_1 moves to the left due to the oxide expansion. The reverse motion occurs during dissolution.

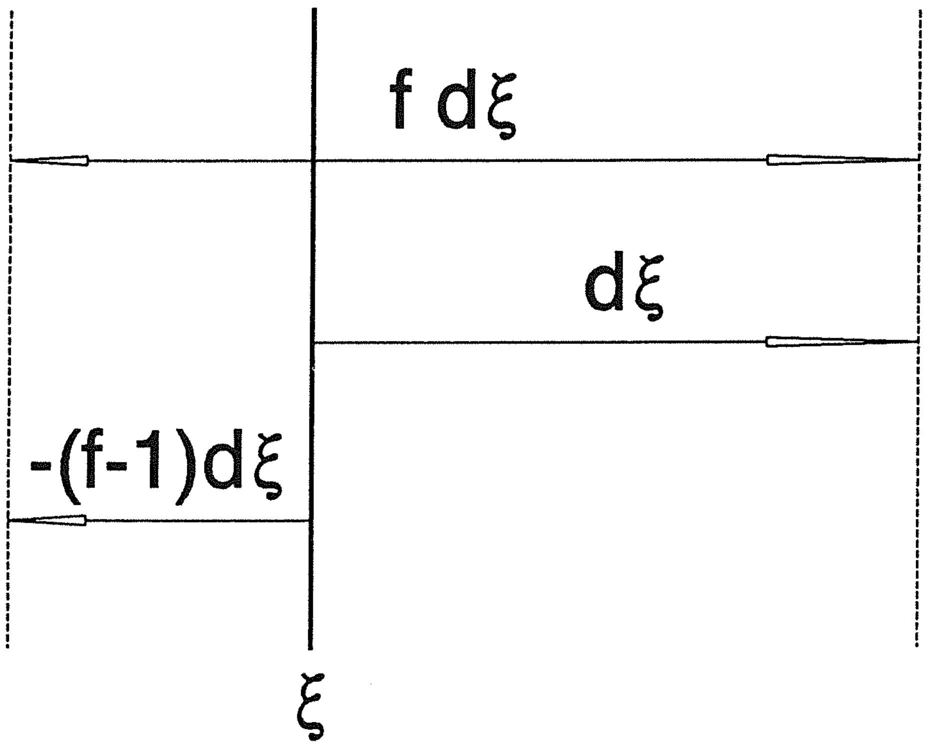

Figure 8 a: Due to oxygen diffusion a layer dξ of α-Zr transforms to ZrO_2. The different density of Zr atoms between both phases is responsible for the expansion and consequent displacement of the oxide as a whole. Something similar happens during the oxide dissolution.

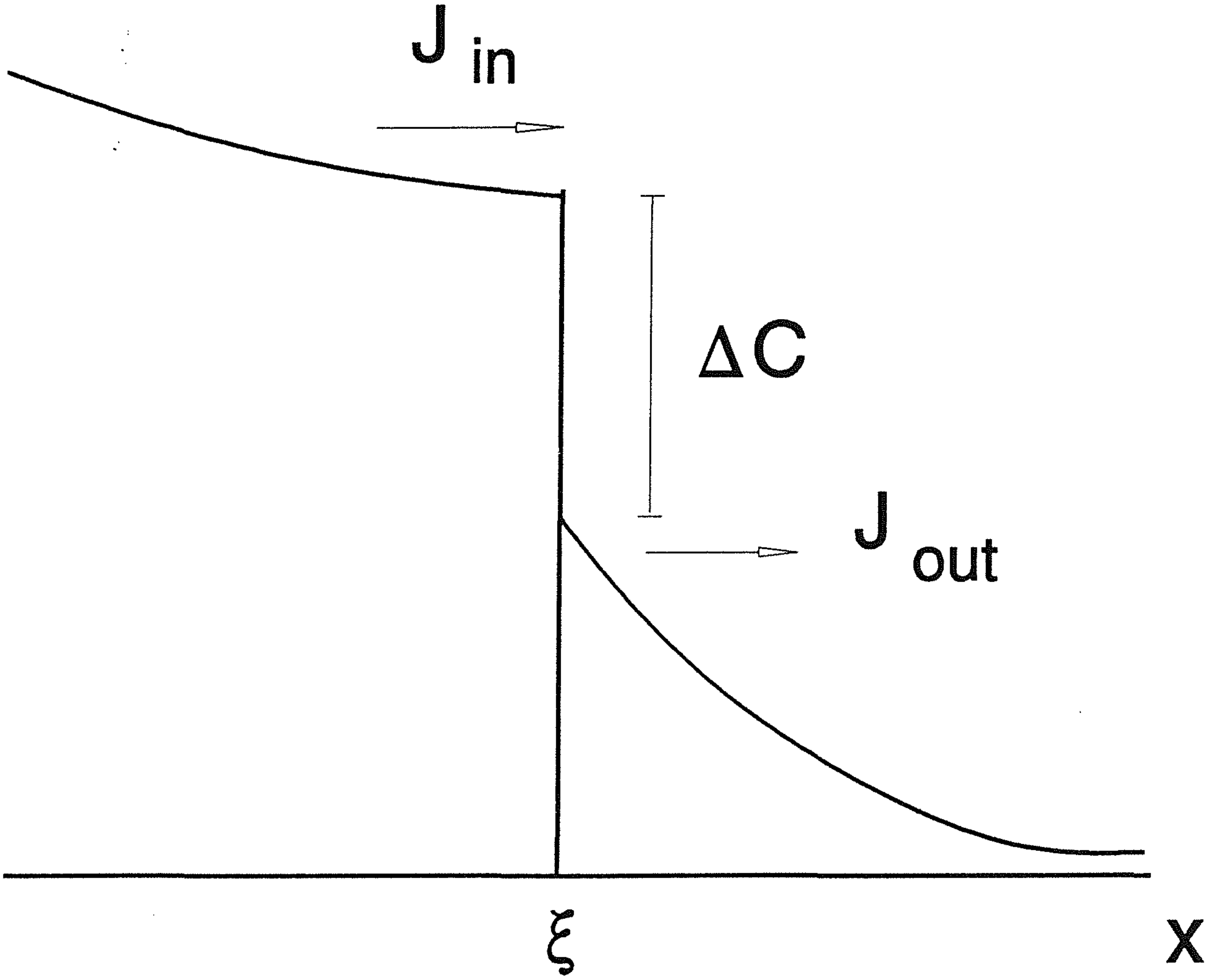

Figure 8 b: The flux of diffusing substance arriving at any interface, J_{in}, is distributed among the flux entering the next phase J_{out} and that necessary to produce the phase change $\Delta C \, d\xi/dt$.

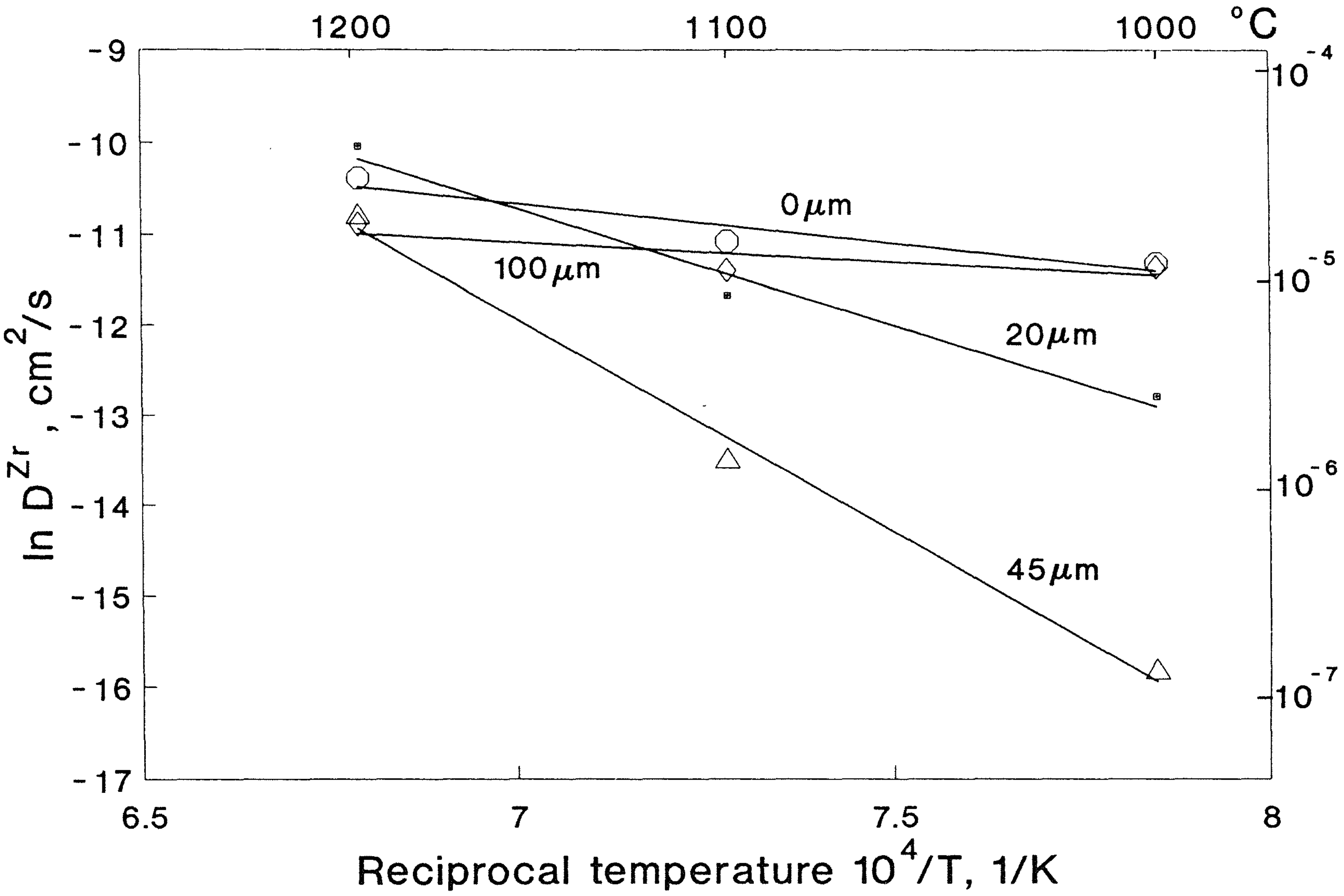

Figure 9 a: Effective diffusion coefficients of Zr in the eutectic for oxide layers of 0, 20, 45 and 100µm.

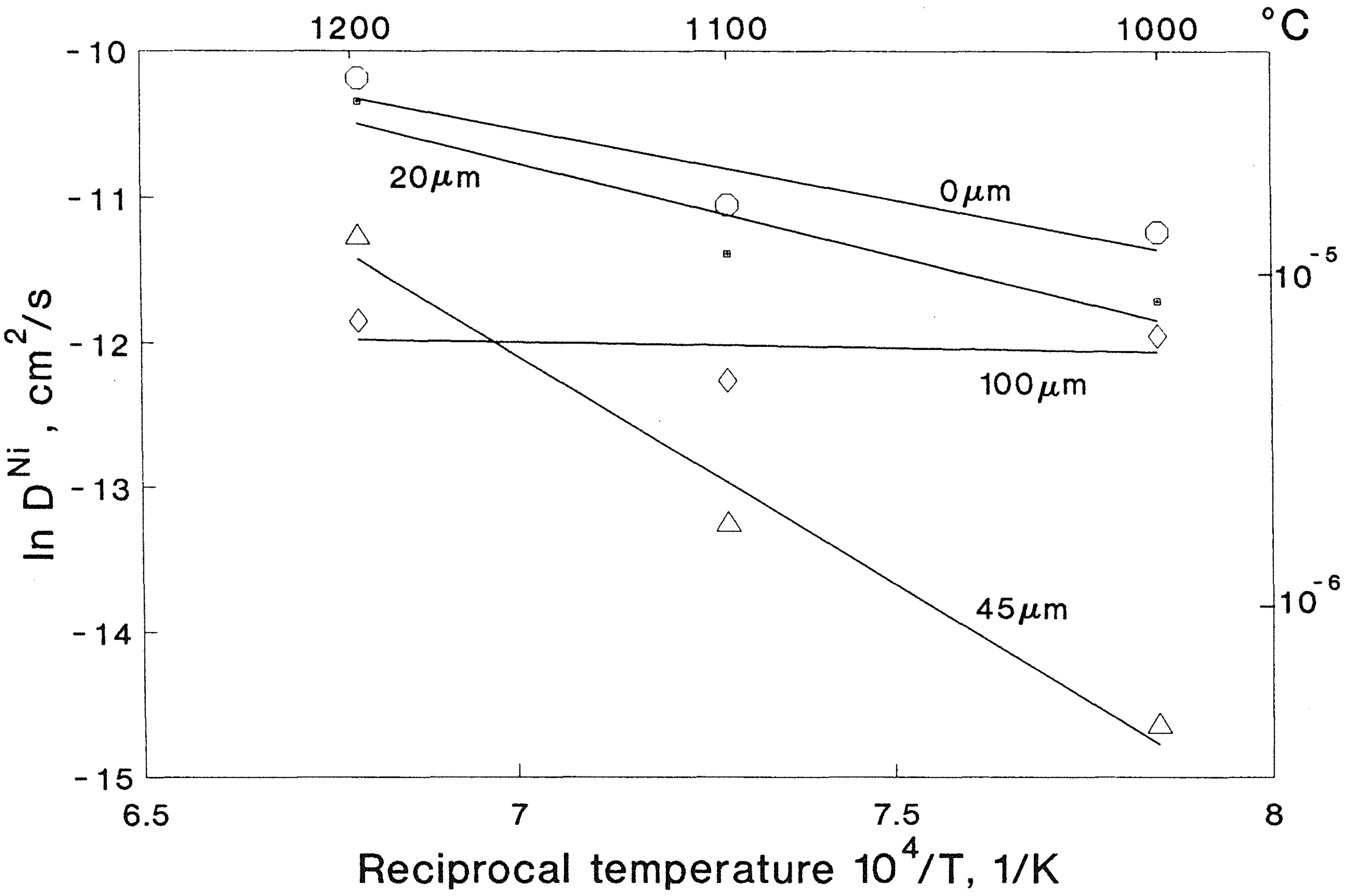

Figure 9 b: Effective diffusion coefficients of Ni in the eutectic for oxide layers of 0, 20, 45 and 100μm.

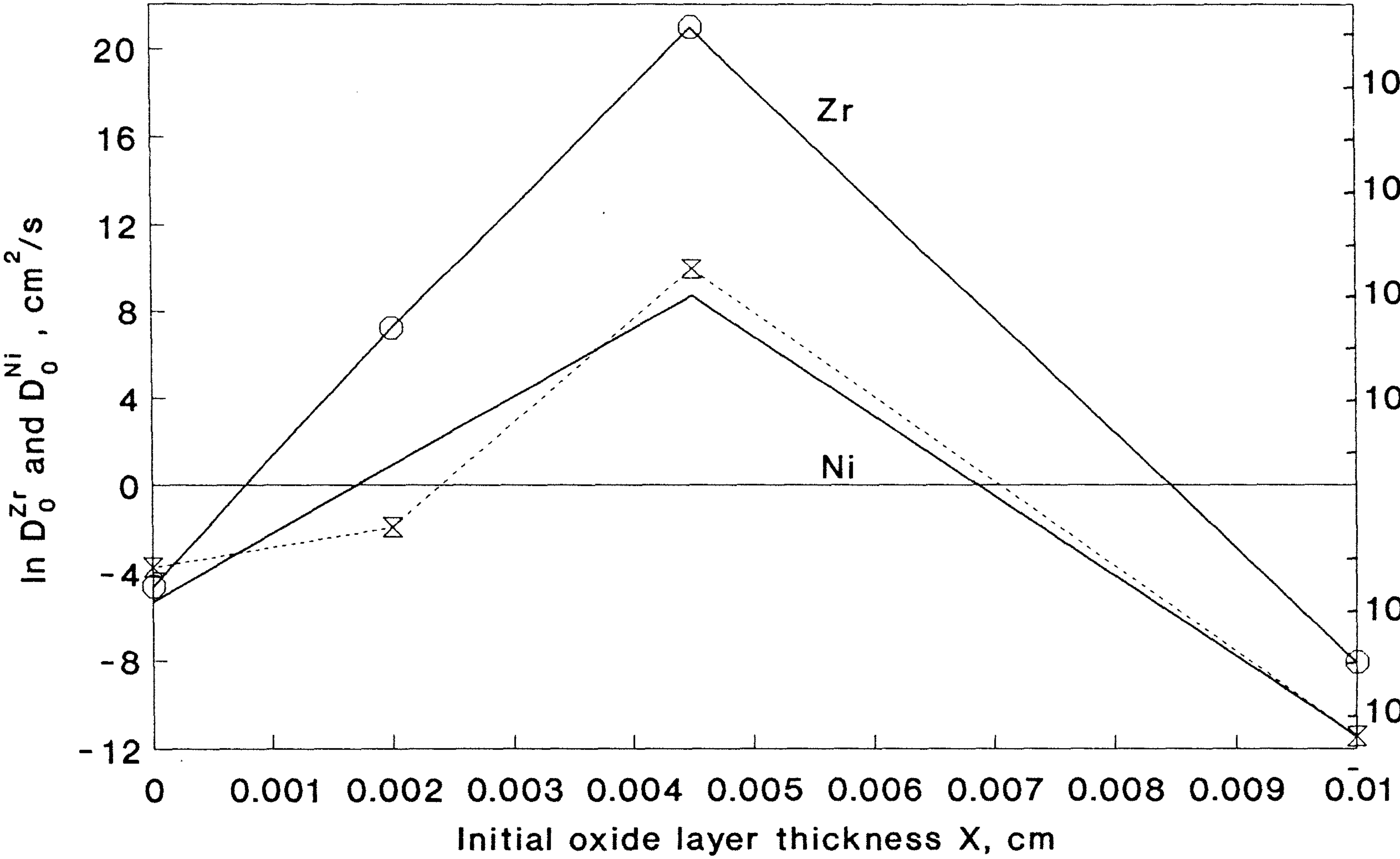

Figure 10 a: Frequency factors of Zr and Ni diffusion, D_0^{Zr} and D_0^{Ni}, for different oxide layer thicknesses.

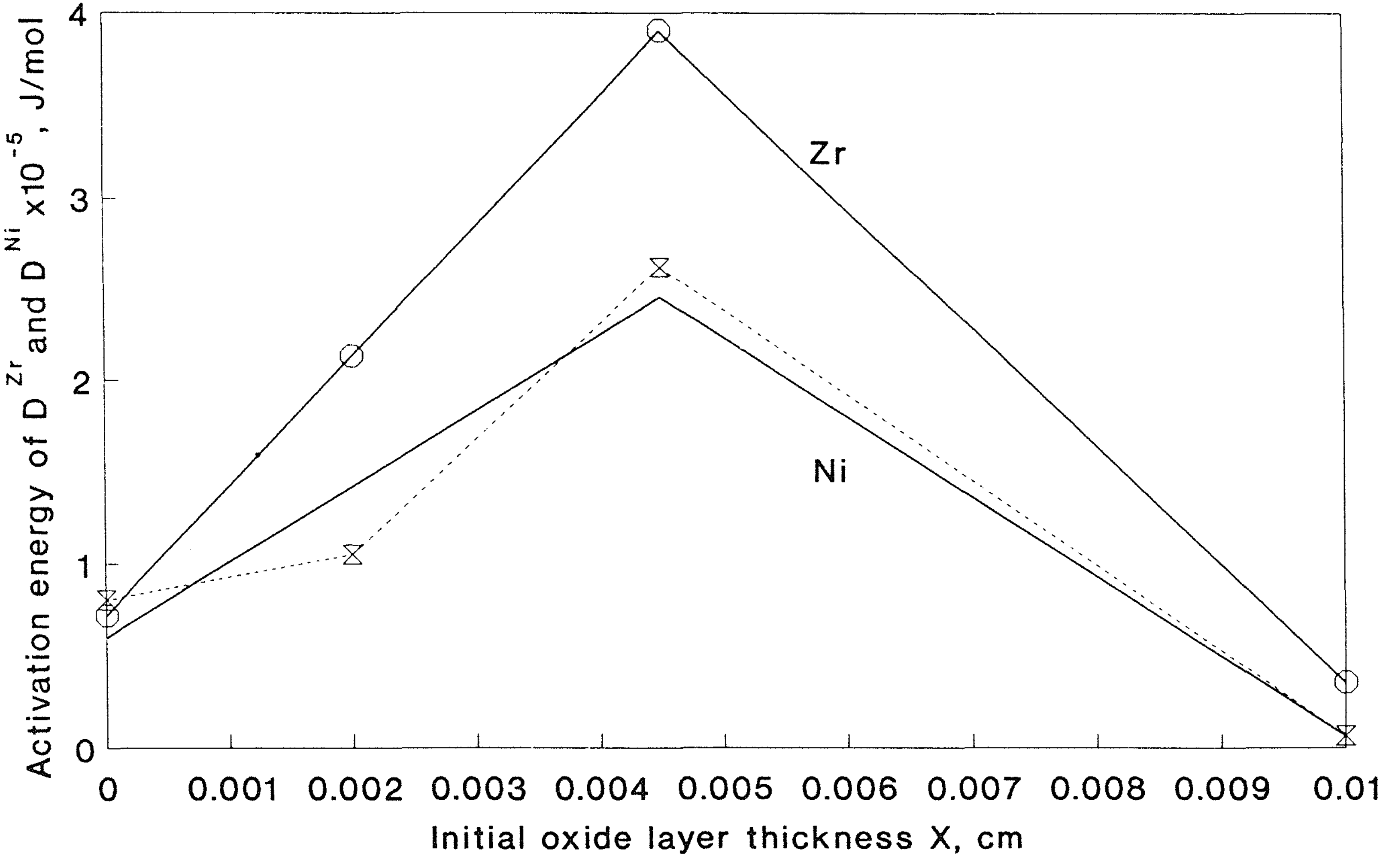

Figure 10 b: Activation energies of Zr and Ni diffusion, Q^{Zr} and Q^{Ni}, for different oxide layer thicknesses.

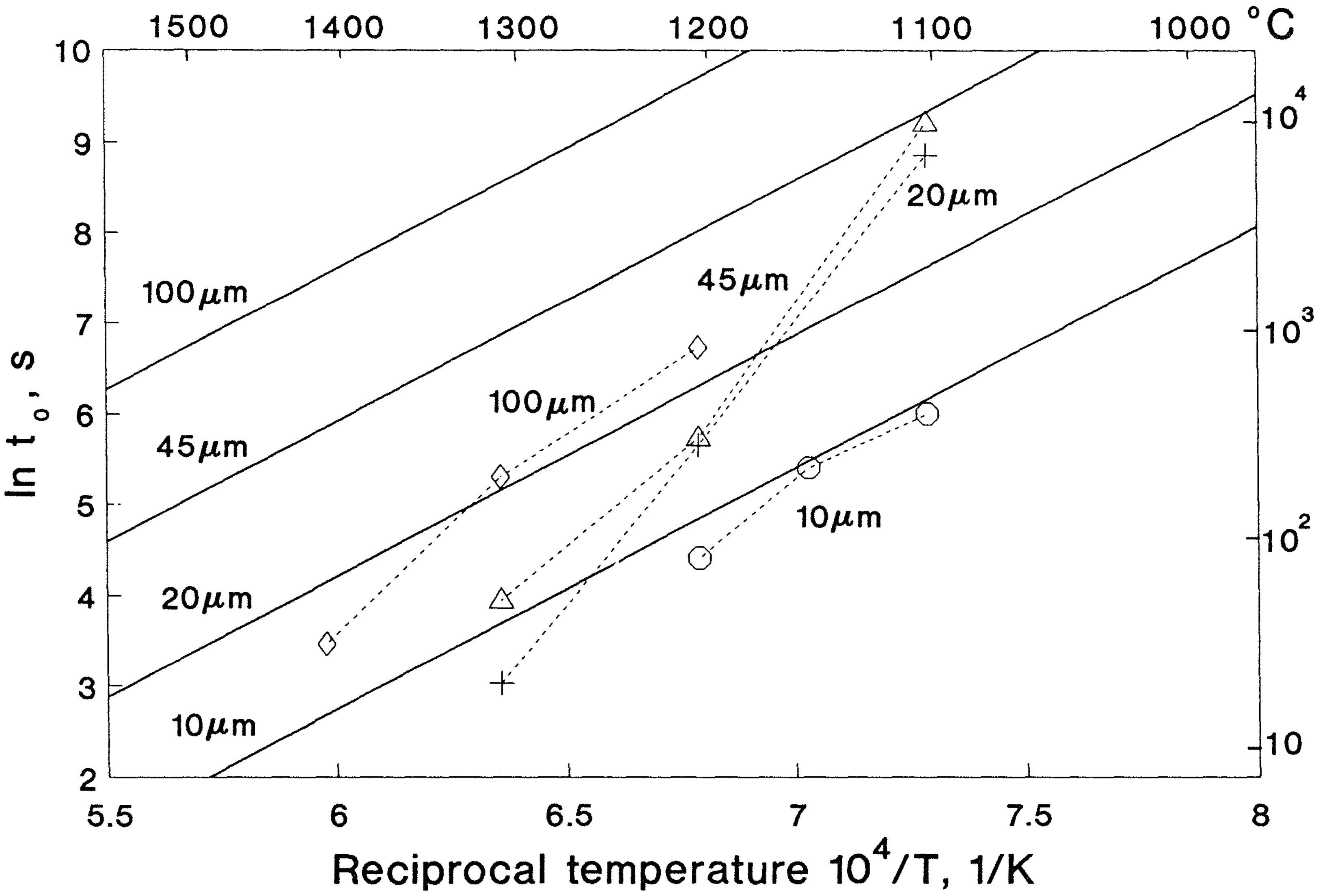

Figure 11: Experimental and calculated results of the delay time for Zircaloy/Inconel interaction as a function of the reciprocal of absolute temperature.

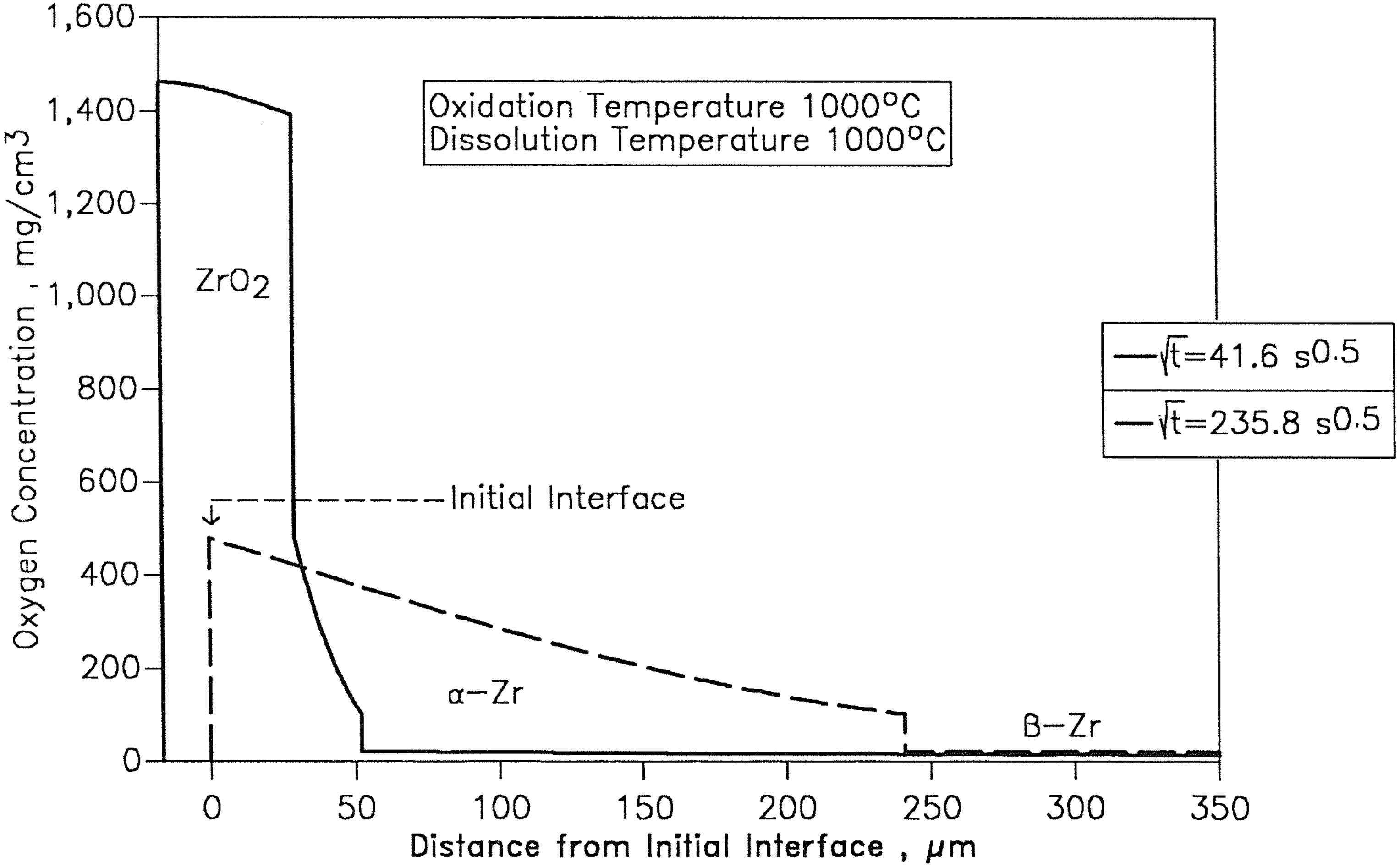

Figure 12: DISOL calculations before (full line) and after (dotted line) ZrO_2 dissolution.

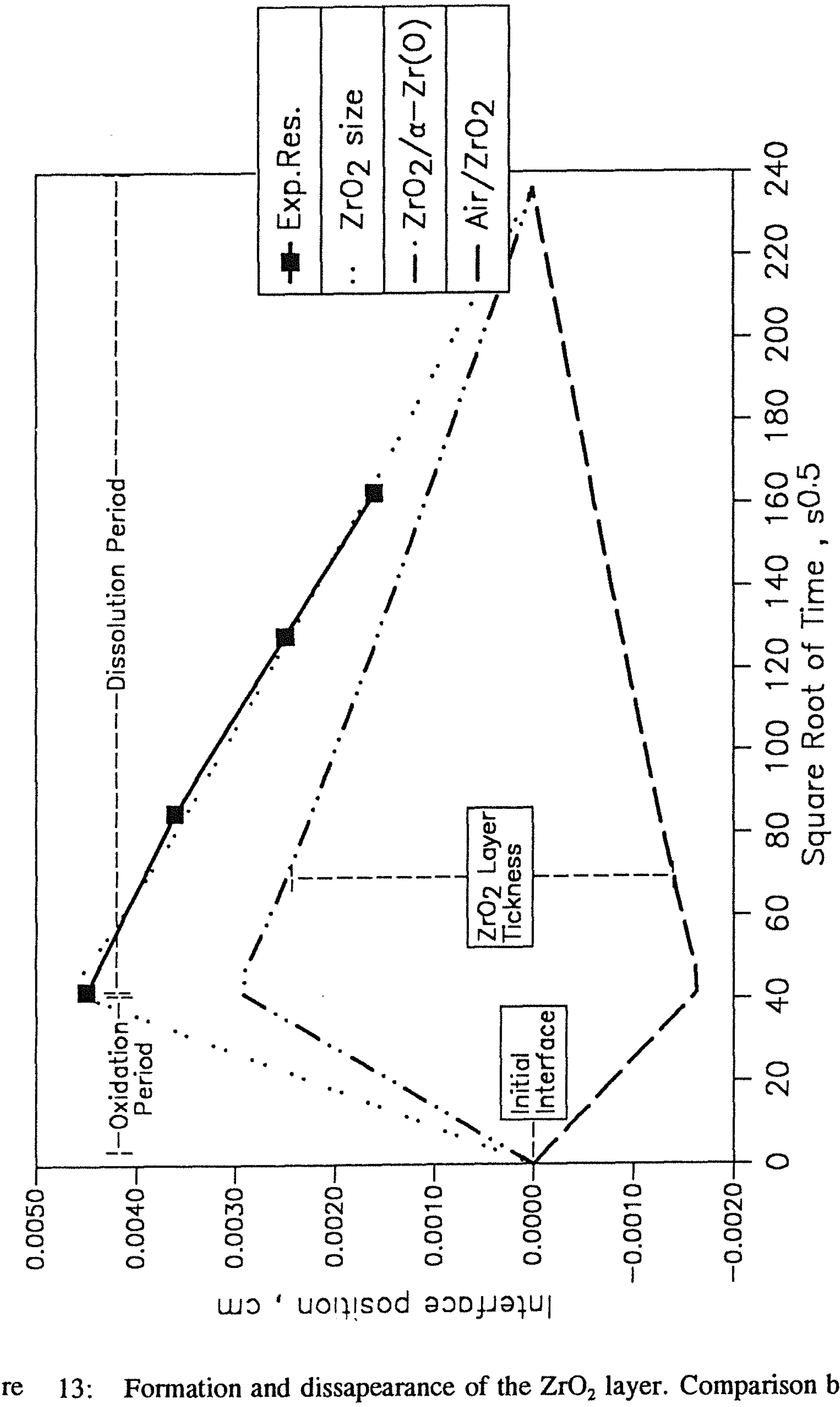

Figure 13: Formation and dissapearance of the ZrO_2 layer. Comparison between DISOL calculations and experimental results at 1000°C.

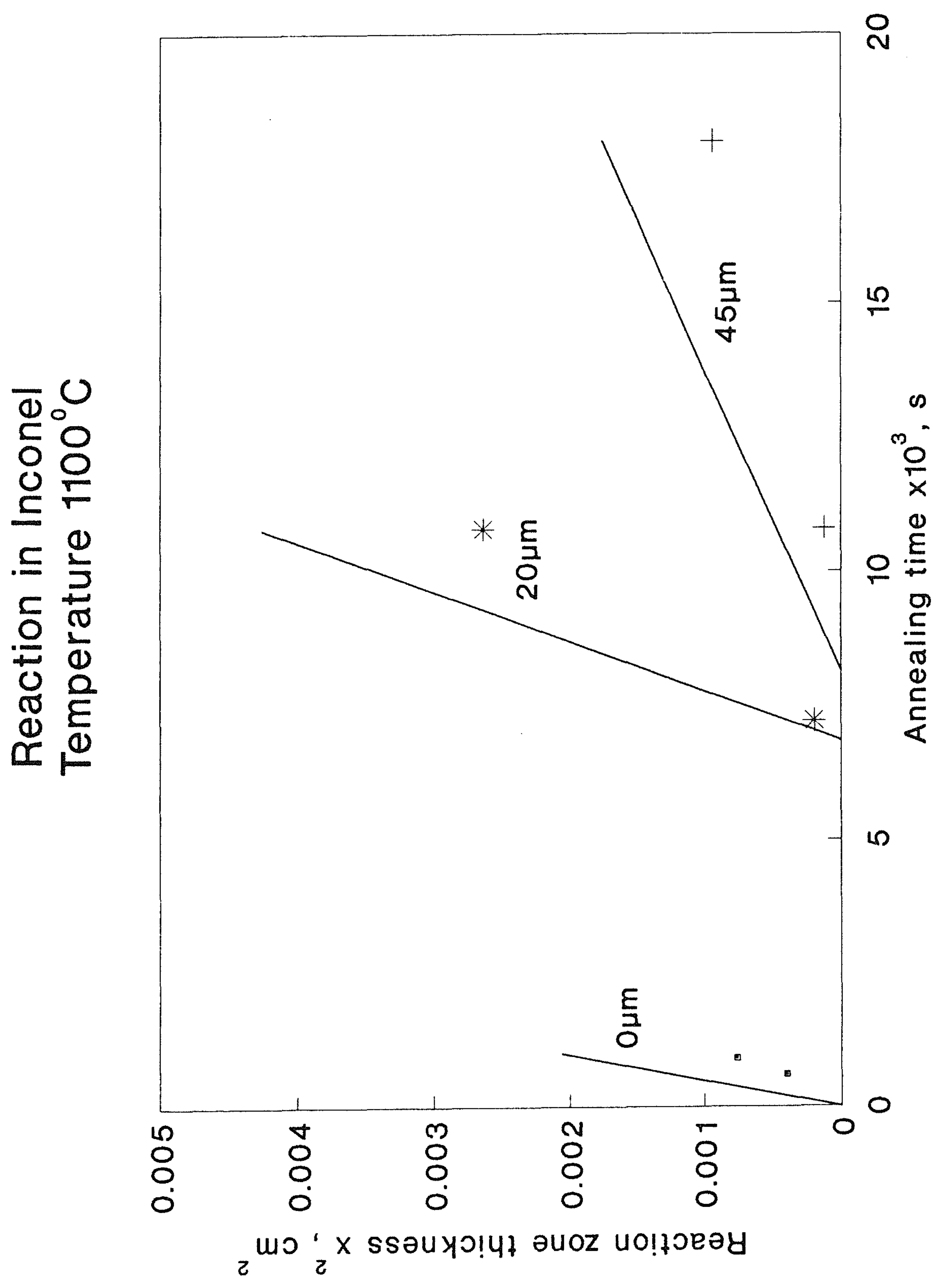

Figure 14 a: Comparison between calculated (full lines) and experimental (points) reacted Zircaloy thickness for the chemical interaction at 1100°C.

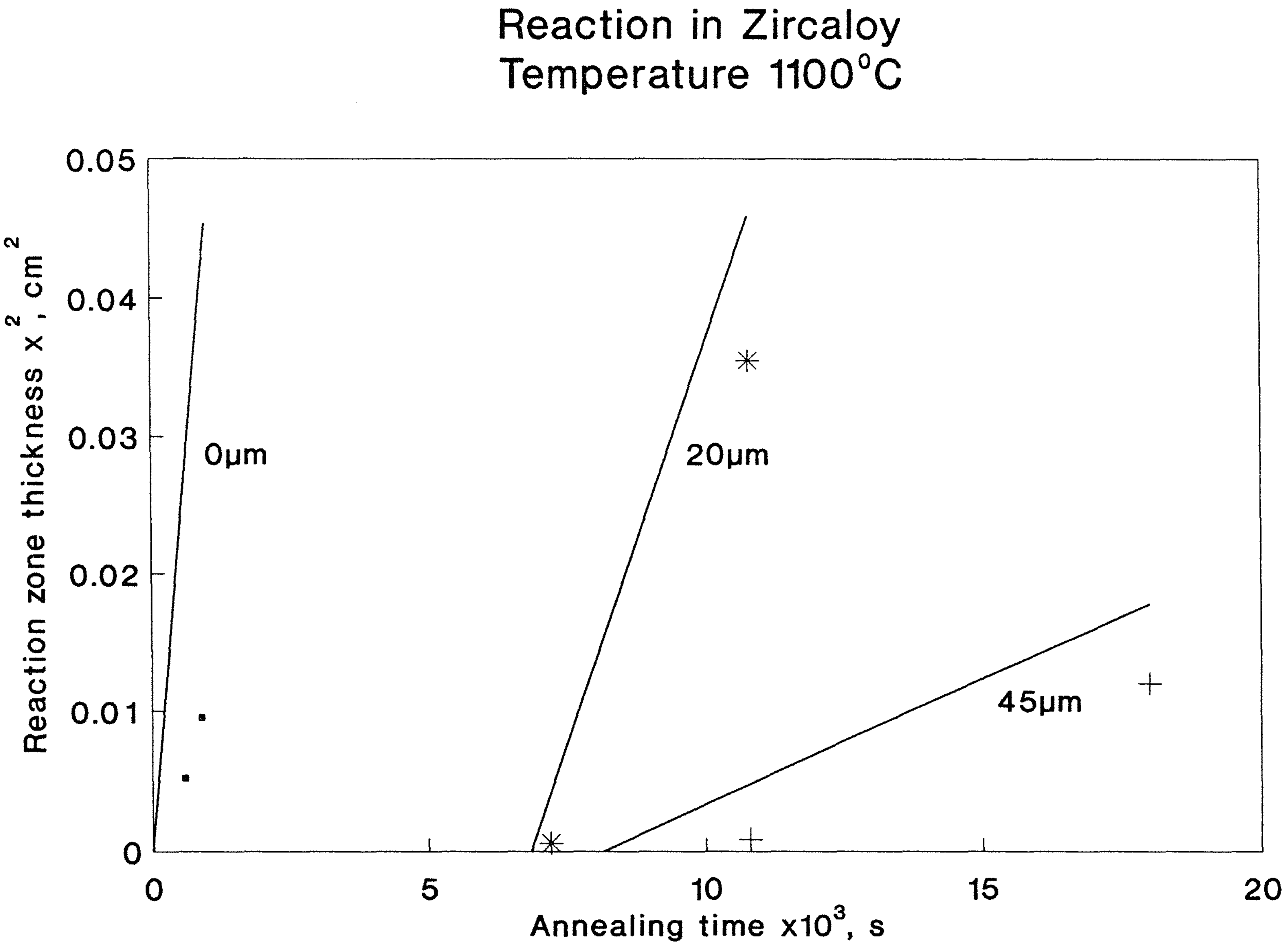

Figure 14 b: Idem Figure 14 a but on the Inconel side.